7-11-2013

Modeling and Analysis of Actinide Diffusion Behavior in Irradiated Metal Fuel

Paul Edelmann

Paul G. Edelmann
Candidate

Chemical and Nuclear Engineering
Department

This dissertation is approved, and it is acceptable in quality and form for publication:

Approved by the Dissertation Committee:

Cassiano de Oliveira, Chairman

Gary W. Cooper

Andrea Alberto Mammoli

Marina Popova

Modeling and Analysis of Actinide Diffusion Behavior in Irradiated Metal Fuel

by

PAUL G. EDELMANN

B.S., Nuclear Engineering, Rensselaer Polytechnic Institute, 1992

DISSERTATION

Submitted in Partial Fulfillment of the
Requirements for the Degree of

Doctor of Philosophy

in

Engineering

The University of New Mexico
Albuquerque, New Mexico

May, 2013

DEDICATION

Amorosamente dedicar esta tesis a mi esposa ya mis hijos hermosos, que me han apoyado en cada paso del camino.

ACKNOWLEDGMENTS

I would like to express my deepest gratitude to my advisor and Committee Chairman, Dr. Cassiano Ricardo Endres de Oliveira, for his excellent guidance, caring and patience through these years with all the changes and for never giving up on me. I would also like to thank my other Committee Members: Dr. Gary W. Cooper, Dr. Andrea Alberto Mammoli, and Dr. Marina Popova, all very kindly having agreed to participate in my final defense.

I will forever be indebted to my wife Elida, and to my three wonderful children, Katrina, Erik and Alexandra. They all helped to make this possible through their love and support.

MODELING AND ANALYSIS OF ACTINIDE DIFFUSION BEHAVIOR IN IRRADIATED METAL FUEL

by

Paul Edelmann

B.S., Nuclear Engineering, Rensselaer Polytechnic Institute, 1992

Ph.D., Engineering, University of New Mexico, 2013

ABSTRACT

There have been numerous attempts to model fast reactor fuel behavior in the last 40 years. The US currently does not have a fully reliable tool to simulate the behavior of metal fuels in fast reactors. The experimental database necessary to validate the codes is also very limited. The DOE-sponsored Advanced Fuels Campaign (AFC) has performed various experiments that are ready for analysis. Current metal fuel performance codes are either not available to the AFC or have limitations and deficiencies in predicting AFC fuel performance. A modified version of a new fuel performance code, FEAST-Metal , was employed in this investigation with useful results.

This work explores the modeling and analysis of AFC metallic fuels using FEAST-Metal, particularly in the area of constituent actinide diffusion behavior. The FEAST-Metal code calculations for this work were conducted at Los Alamos National Laboratory (LANL) in support of on-going activities related to sensitivity analysis of fuel performance codes. A sensitivity analysis of FEAST-Metal was completed to identify important macroscopic parameters of interest to modeling and simulation of metallic fuel performance. A modification was made to the FEAST-Metal constituent redistribution model to enable accommodation of newer AFC metal fuel compositions with verified results. Applicability of this modified model for sodium fast reactor metal fuel design is demonstrated.

TABLE OF CONTENTS

LIST OF ACRONYMS AND ABBREVIATIONS vii

CHAPTER 1. INTRODUCTION 1

CHAPTER 2. THE FEAST-METAL FUEL PERFORMANCE CODE 11

CHAPTER 3. FEAST-METAL PARAMETER SENSITIVITY STUDY 16

CHAPTER 4. FEAST-METAL CONSTITUENT REDISTRIBUTION MODEL ... 33

CHAPTER 5. RESULTS 42

CHAPTER 6. DISCUSSION AND CONCLUSIONS 46

REFERENCES 48

LIST OF ACRONYMS AND ABBREVIATIONS

1D	One-Dimensional
3D	Three-Dimensional
AEC	Atomic Energy Commission
AFC	Advanced Fuels Campaign
AFCI	Advanced Fuel Cycle Initiative
Am	Americium
ANL	Argonne National Laboratory
Ar	Argon
BU	Burnup (A measure of fuel exposure and fissile depletion)
CDF	Cumulative Damage Fraction
CPU	Central Processing Unit
DOE	Department of Energy
EBR-II	Experimental Breeder Reactor-II
EDF	Electricité de France
FCCI	Fuel Clad Chemical Interaction
FCMI	Fuel Clad Mechanical Interaction
FE	Finite Element
FEAST	Fuel Engineering And Structural analysis Tool
FEAST-METAL	The metal fuel version of FEAST code

GRSIS	Gas Release and Swelling in ISotropic fuel matrix
He	Helium
INL	Idaho National Laboratory
Kr	Krypton
LANL	Los Alamos National Laboratory
LWR	Light Water Reactor
M&S	Modeling and Simulation
MIT	Massachusetts Institute of Technology
MOX	Mixed Oxide Fuel
Na	Sodium
Np	Neptunium
PCI	Pellet-Clad Interaction
PIE	Post-Irradiation Examination
Pu	Plutonium
PWR	Pressurized Water Reactor
U	Uranium
US	United States
Xe	Xenon
Zr	Zirconium

CHAPTER 1. INTRODUCTION

Interest in sodium-cooled fast reactors for long term actinide management and energy production [18] has been revived and renewed by the development of recent US Department of Energy Programs such as the Advanced Fuel Cycle Initiative (AFCI). Analyses of these complex systems require the coupling of diverse fields, such as thermal-hydraulics, neutronics, structural mechanics and fuel behavior.

Advancing the performance of advanced nuclear fuel cycles and advanced reactors requires enhancing our fundamental understanding of fuel and materials behavior under irradiation. The capability to accurately model the nuclear fuel systems and understand fuel behavior under normal and accident operating conditions is critical. The Advanced Fuels Campaign (AFC) is implementing a goal-oriented and science based implementation strategy. This strategy includes theory, experiment and modeling and simulation components. The experimental program includes a small-scale experiments program aimed at understanding isolated phenomena and measurements of material properties while integral tests are still required for fuel qualification. Recent advances in computer and mathematical sciences will be used to integrate the mathematical models developed for various phenomena to predict the integral behavior of the system at various scales. In early phases of the development, the modeling and simulation (M&S) tools will be used to address the scaling issues when large-scale applications are considered. The M&S tools based on the validated theory and small-scale experiments will be used to minimize the need for large-scale experiments before deployment.

The prediction of fuel behavior under irradiation involves very complex material behavior that is not seen in any other engineering discipline. The understanding of fundamental mechanisms driving damage production and evolution is not at a desirable level of maturity and, in some cases, does not exist. To make advances toward the development of predictive tools, it is clear that we need high-performance M&S techniques. The recent advances in computer hardware and simulation algorithms now enable us to simulate the atomistic and meso-scale behavior of materials, including

radiation-induced damage at submicron scales, with the desired level of accuracy and computational efficiency.

It is also important to recognize that the fuel-clad interactions are primarily 3D in nature. It would be highly desirable to have advanced three-dimensional fuel performance codes, and such M&S tools will be developed eventually. Until that happens, we have the 1D capability of current models for steady-state and some transient performance calculations. Most material properties are affected by the microstructure characteristics of the materials. Predictions of transient behavior and fuel compressibility and fragmentation (especially for oxide fuels) will require microstructural-based swelling modeling approaches to account for the micro-chemical behavior of the fuel.

Four types of fuels have been considered for fast reactor applications. They are oxide, metal, carbide and nitride fuels. Each fuel type has advantages and disadvantages with respect to the others. With the success of the metal and oxide fuels demonstrated through the 1980s and early 1990s, a considerable infrastructure and knowledge base has been accumulated to support these two fuel types, while the interest in the more problematic carbide and nitride fuels has faded in the United States [18].

Metal fuel advantages

In a fast neutron reactor, the minor actinides produced by neutron capture of uranium and plutonium can be used as fuel. Metal actinide fuel is typically an alloy of zirconium, uranium, plutonium and the minor actinides. It can be made inherently safe as thermal expansion of the metal alloy will increase neutron leakage.

The fuel/clad gap is filled with liquid sodium, which acts as a thermal bond. Metal fuel has other attractive characteristics as well. It has high thermal conductivity, which, combined with a highly conducting gap, maintains low fuel temperatures and reduces stored energy, an important feature during transients, such as the unprotected loss of primary flow and loss of heat sink. High heavy metal density and low moderating power provide for a harder spectrum and excellent neutron economy. Low fuel clad mechanical

interaction (FCMI) at the upper part of the fuel pin enables achievement of high burn-up. Metal fuel also has good compatibility with the coolant, and facilitated manufacturing and reprocessing by electrochemical methods. Oxide fuels have none of these advantages for fast reactor application.

Literature Review and Current/Prior Work

Current capabilities are focused on fuel pellets, although it is known that the limiting phenomena could be associated with the behavior of the fuel assembly (assembly bowing, etc.). It is possible to design a fuel pellet for 40% burn-up, although this design may result in failures at much lower burn-ups because of 3D assembly distortions when it is placed in an assembly for many reasons [13]. In addition, despite the fact that multiple computer codes are developed by many researchers, a robust predictive capability for quantifying fuel behavior and its uncertainty is still lacking. Large uncertainties and scatter still exist in the predictions, mainly because:

- Fuel rods are 3D structures, and large deformations may occur.
- Fuel assemblies are 3D structures and can behave differently from a single fuel pellet.
- The constitutive materials laws are nonlinear as a result of creep, plasticity, and other material data.
- Material behavior is anisotropic and time dependent.
- Material behavior is not fully understood.
- The science of irradiation effects on materials is not mature and is not well understood.
- The fundamental data to verify materials modeling is lacking (in some cases, data cannot be taken directly, only indirectly).
- The physical process involved makes it difficult to define separate effects testing by controlling the boundary conditions to validate materials models.
- Processes under irradiation conditions occur in a wide variety of time and length scales, each requiring different modeling techniques.
- Integrated multiscale, multiphysics modeling (that covers all scales) is lacking.

The most desirable approach in fuel modeling is to develop predictive tools with 3D capabilities because the location of fuel-cladding contact becomes critical for fuel-cladding chemical interactions. Some recent attempts have been made to create 3D codes with varying degrees of sophistication [13].

Michel et al. reported on software (PLEIADES) [14] that is developed by the Atomic Energy Commission (AEC) and Electricité de France (EDF). This software includes a multidimensional finite element (FE) program (ALCYONE) [15], devoted to pressurized-water-reactor (PWR) fuel rods. Pellet clad interaction (PCI) studies are mainly undertaken with the 3D model of ALCYONE. The objectives of their work is twofold: (1) to propose a constitutive model for the fuel pellet, which accounts for the stress relaxation of the material resulting from cracking and creep; and (2) to estimate the impact of the pellet cracking on PCI.

The most recent results on the 3D thermo-mechanical model of fuels are reported by Newman [13], who developed a 3D thermo-mechanical model that is fully coupled to an oxygen diffusion model for both steady-state and transient cases.

The Nuclear fuels are generally in two forms, excluding some special cases for special reactors, oxide ceramic fuels, and metal fuels. LWR technology uses ceramic uranium oxide fuels, with explorations into mixed plutonium-uranium oxide (MOX) fuels. The oxide and metallic uranium, uranium-zirconium, and uranium-zirconium-plutonium fuels are currently used in the fast-reactor program. Commercial nuclear reactor fuel design employs a simple design concept, that is, cylindrical fuel pellets with diameters in the range of 5 to 12 mm. These are inserted into a 1 to 4-m long zircalloy-based annular tube (clad) in such a way that there is a small gap between the fuel pellets and zircalloy cladding. The zircalloy cladding is used to contain volatile fission products such as Xe, He, Kr, etc., within the plenum space above the fuel pellets. The gap and plenum are initially filled with pressurized helium. The cladding is the first safety barrier, preventing radioactive fission release into the coolant, which would contaminate the primary loop components in the event of failure. Similar concepts are applied to fast reactor fuels with some modifications, such as shorter fuel rod lengths and different gap

fillings (liquid sodium for metal fuel and helium for oxide fuel). The metal fuel in a fast reactor is composed of a single rod, rather than a collection of several hundred individual pellets. The fuel pins (or rods) are bound together in an assembly (or bundle) and separated with either grid spacers or wire-wraps, which constrain the pins radially, as well as inducing mixing and turbulence in the coolant. In some reactor concepts, these are contained within a can of structural material for enhanced flow control.

Although their mechanical design is simple, the thermo-mechanical behavior of a nuclear fuel pellet or rod (the fuel assembly is more complex geometrically) involves a complex system of interacting, competing, and conflicting processes as a result of the high thermal-power densities and irradiation. Various fuel and reactor types have different processes that must be modeled. However, all have some common engineering characteristics with respect to heat transfer, solid mechanics, chemical transport, neutronics, and fluid flow – all of these are driven by the physical mechanisms taking place at the microstructure level (i.e., at the grain, or subgrain scale). The low conductivity of ceramic fuels, for example, yields a steep radial temperature profile in the fuel element. As a result, the fuel element experiences thermal stresses causing pellet cracking and redistribution. Migration of porosity and fuel constituents and fission products cause fuel restructuring in both metal and oxide fuels. The irradiation and fission product, as well as the chemical interaction, changes the material properties of the fuel and cladding. The microstructural characteristics and their evolution with fuel and cladding irradiation can also influence these properties. Fuel swelling is a result of fission products, both gaseous and solid, and atomic displacements due to the neutron flux influence on the dimensional changes and mechanical properties of the materials. Swelled fuel causes a mechanical interaction between fuel and cladding that can produce stresses and deformation in addition to the stress caused by internal pressure in the fuel. The nuclear (heat and irradiation) source drives many of these processes, which can be greatly variable in thermal reactors. In addition, the chemical interactions between cladding and coolant significantly affects the heat transfer coefficient and mechanical strength of the cladding; these interactions can be driven by both local (nucleate boiling) and global (soluble metals) coolant flow conditions.

Metal fuel typically consists of a binary alloy of uranium and zirconium or a ternary alloy of uranium, plutonium and zirconium. The addition of americium, neptunium, and curium to the traditional metallic fuel is considered in the AFC. These actinides add further complications to the fuel behavior. For example, it is known from limited data that americium acts like zirconium and diffuses toward the center of the fuel with slower rates. Neptunium is observed to act like plutonium, which does not significantly diffuse. The weight fractions of uranium, plutonium, zirconium, americium, and neptunium in the AFC fuels vary; minimum and maximum values of weight fractions are given in Table 1.

Table 1. Minimum and Maximum Weight Fractions of AFC Metallic Fuels

	U	Pu	Zr	Am	Np
Max.	0.70	0.6	0.6	0.12	0.1
Min.	0.3	0.2	0.1	0.03	0.01

However, various phenomena limit the in-core performance of metal fuel assemblies, including clad thermal, irradiation creep, void swelling, fuel restructuring, and Fuel-Clad Chemical Interaction (FCCI). It is clear that any credible attempt at assessing the performance of metal fuel must include a model that is able to predict the temperature, stress, and strain time-dependent distributions within the clad and fuel for given operating and abnormal conditions. This model should include the effects of fuel restructuring, FCCI, thermal expansion, thermal creep, irradiation creep, fuel swelling, and fission gas release.

Metallic fuel undergoes various stages during irradiation. At the beginning of metal fuel irradiation (up to 1% BU), swelling causes grain boundary tearing and cracking, the fuel reaches the clad, and the fuel becomes axially restrained at the “hot” axial location. The resulting axial friction force is enough to stop the axial growth of the fuel by compressing the existing open gas pores. Furthermore, the swelling rate is reduced because of the axial frictional force. The radial contact pressure between the fuel and clad is low because of the extrusion of the inner zone fuel into the cracks. The fission gas release into the plenum begins.

Between 1% and 2% BU, cracks are closed and fuel becomes both axially and radially restrained at the hot axial location. The radial contact pressure between the fuel and clad rises to a level somewhat higher than the plenum pressure. Open gas pores start to be compressed to accommodate solid/liquid fission product swelling. The fission gas release fraction rises rapidly to 5%. At higher burn-ups between 2% and 13%, the contact pressure holds at a level somewhat higher than the plenum pressure as the open pores are further compressed to accommodate the accumulation of solid products. Finally, at higher burn-ups (>13%), fuel does not have enough open pores to accommodate solid fission product accumulation. The resulting fuel-clad contact pressure rises significantly. When open pores are <5%, the contact pressure rises rapidly and a breach may result.

Table 2 shows the key models in various metal fuel performance codes.

Table 2. Key Modeling in Metal Performance Codes [1]

Key Models	LIFE-METAL (Steady-State and Design Basis Accidents)	SESAME (Steady-State)	ALFUS (Steady-State)	MACSIS (Steady-State)	FEAST-METAL (Steady-State and Transients)
Developer	ANL	CRIEPI	CRIEPI	KAERI	MIT
Fission Gas Release and Fuel Swelling	Empirical Correlation	Empirical Correlation	Mechanistic Model, based on UO2 Fuel	Mechanistic Model, based on UO2 Fuel	Mechanistic Model, based on Metallic Fuel
Species Transport	Empirical Correlation	Chemical Equilibrium Model	Thermo-transport theory	Thermo-transport theory	Thermo-transport theory
Temperature Distribution	1D Model	1D Model	1D Model	1D Model	1D Model
Mechanical Analysis	1D Model	1D Model	2D Model	1D Model	1D Model
FCCI	Empirical Correlation	N/A	Empirical Correlation	N/A	Diffusion Model based on Precipitation Kinetics
Creep Fracture	Cumulative Damage Fraction Model	N/A	N/A	N/A	(1) Cumulative Damage Fraction Model (2) Constrained Diffusional Cavity Growth Model

Experimental Work

EBR-II

The EBR-II experiments emphasized testing fuels and materials for future, larger, liquid metal reactors in the radiation environment of the EBR-II reactor core, which was operated as the Integral Fast Reactor prototype until 1994. Results from 6 fuel pins irradiated in some of the EBR-II experiments were used in the FEAST-Metal sensitivity analysis as the first phase of this research. Benchmarks originally used to validate the FEAST-metal code were used in part to verify the modified FEAST constituent redistribution model in the second phase of this research.

AFC

The AFC rodlet assembly is designed to be a miniature fast-reactor fuel rod having a standard diameter and reduced length. The rodlet assembly consists of the metallic fuel column, sodium bond, stainless-steel Type 421 (HT9) cladding, and inert

gas plenum. A stainless-steel capsule assembly contains a vertical stack of six rodlet assemblies. The rodlet and capsule designs and dimensions are shown in Figures 1a and 1b [16]. AFC fuel is typically composed of U-Pu-Zr with some minor actinides, as described in Table 1. It also has a higher Zr content than EBR-II fuel did (up to 60 weight percent), which invalidated the original FEAST model for AFC fuel. This necessitated a modification to the constituent redistribution model in order to enable FEAST-Metal to accommodate AFC fuel compositions.

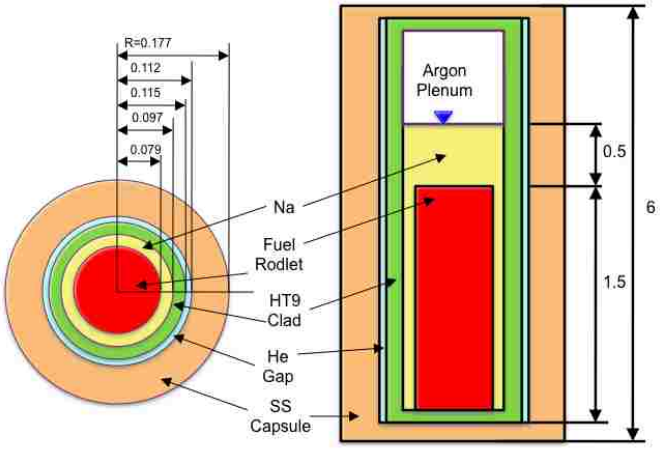

Figure 1a. Typical AFC rodlet design and dimensions [16].

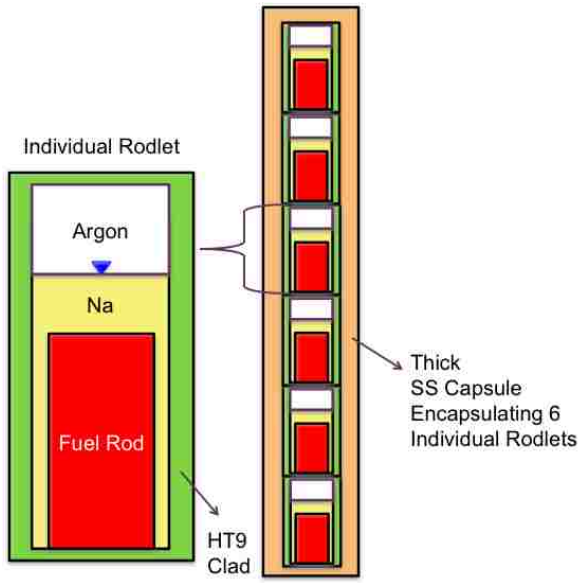

Figure 1b. Typical AFC rodlet capsule design [16].

Research Objectives

AFC has performed various experiments that are ready for analysis. Most current metal fuel performance codes are either not available to AFC or have limitations and deficiencies in predicting AFC fuel performance. Advanced codes such as BISON are still under development and need to be adapted and tailored to AFC analysis needs. FEAST has certain advantages which are not present in other available M&S codes. This work implements a modification to the FEAST-Metal model for constituent redistribution and migration. This model is assessed against AFC test results to identify the need for any further model adjustment, and to determine its usefulness in the design of sodium-cooled fast reactor fuels. Ultimately, 3D codes will be developed to predict AFC fuel performance when fuel composition is varied. For the purpose of this study, the immediate need is to determine and understand fuel constituent and actinide species migration and redistribution under various irradiation conditions, and to establish the ability to predict this behavior in AFC metallic fuels.

Summary of Work Performed and Expected Contributions

In the first phase of this work, a sensitivity study (Chapter 3) was performed on the thermo-mechanical models of FEAST-Metal, producing a reduced set of calibration parameters for possible adjustment in follow-on studies. A modification was then made to the constituent redistribution model (described in Chapter 4) to enable the code to properly handle metallic fuel with composition similar to that of AFC fuel. Results obtained after running the model on EBR-II and AFC fuel input specifications are presented in Chapter 5, and assessment and discussion are provided in Chapter 6.
It is expected that this work will result in:

- Enhanced understanding of irradiated material behavior, especially diffusion of actinides in metal fuel;
- Improved capability for predicting this behavior in AFC metal fuel.

CHAPTER 2. THE FEAST-METAL FUEL PERFORMANCE CODE

FEAST-METAL is a fuel performance code developed for predicting steady state and transient behavior of U-Pu-Zr metallic fuel alloys with stainless steel clad in sodium fast reactor environments. The code currently adopts HT9 cladding properties. The code includes several physics based mechanical and semi-empirical continuum level models to predict various important phenomena occurring under normal and off-normal scenarios. Details of the physical models can be found in Karahan [17]. The included models are: Fission Gas Release and Swelling, Constituent Redistribution, Temperature Distribution, Fuel Clad Chemical Interaction, Mechanical Analysis, and Transient Creep Fracture.

The FEAST code was developed for analysis of the steady-state and transient irradiation behavior of U-Zr and U-Pu-Zr metal fuels. It was designed to be highly flexible, so that constitutive models for other alloys of interest (e.g., TRU-Zr alloys) can be easily added to the code. FEAST's mechanical model is similar to the respective LIFE code algorithm. Variation of material properties (fuel creep, thermal expansion, Young's modulus) with local fuel composition is taken into account. The fuel and cladding regions can be divided into up to 8 radial nodes each; however, six radial nodes in the fuel region and at least two radial nodes within the cladding region are recommended. Axial nodes are also user specified. A maximum of twenty nodes can be assigned in the axial direction. Axial heat conduction is neglected. The fission gas release and swelling module implements the GRSIS algorithm [21] which was originally developed for metal fuel. The fuel constituent redistribution model is based on thermo-transport theory. Empirical models developed for the compressibility of open pores and anisotropic deformation of the fuel slug in ALFUS [22] are implemented into the FEAST-METAL code. Furthermore, an FCCI model based on precipitation kinetics was developed to model cladding wastage. Another important model is the creep-fracture of the clad during transients. It uses the diffusional constrained cavity growth model.

FEAST-METAL has been benchmarked against the available EBR-II database for steady state and furnace tests (transients). The results show that the code is able to predict important phenomena such as cladding strain, fission gas release, clad wastage, clad

failure time and axial fuel slug deformation, satisfactorily.

Thermo-mechanical Behavior of Metal Fuel

Table 3 lists the sequence of key physical phenomena during the irradiation of a typical metal fuel pin, as deduced from the operating experience in the EBR-II reactor at ANL-West in Idaho.

Table 3. Description of the burnup history (72 % smear density U-19Pu-10Zr Fuel)

Burnup (at %)	**Relevant phenomena**
0.0	Irradiation begins
0.5-1.0	(1) Due to swelling, grain boundary tearing and cracking, the fuel reaches the clad and becomes axially restrained at the 'hot' axial location. (2) Resulting axial friction force is enough to stop the axial growth of the fuel by compressing the existing open gas pores. Furthermore, swelling rate reduces due to axial frictional force. (3) The radial contact pressure between fuel and clad is low due to extrusion of the inner zone fuel into the cracks. (4) Fission gas release into the plenum begins.
1.0-2.0	(1) Cracks are closed and fuel becomes both axially and radially restrained at the hot axial location. (2) Radial contact pressure between fuel and clad rises to a level somewhat higher than plenum pressure. Open gas pores start to be compressed to accommodate for solid/liquid fission product swelling. (3) Fission gas release fraction rises rapidly to 50 %.
2.0-13.0	Contact pressure holds at a level somewhat higher than the plenum pressure as the open pores are further compressed to accommodate accumulation of solid products.
13-20	Fuel does not have enough open pores to accommodate solid fission product accumulation. The resulting fuel-clad contact pressure rises significantly. When open pores are less than 5 %, the contact pressure rises rapidly and breach may result.

FEAST-Metal Code Structure

This section provides a detailed description of the FEAST-METAL code structure. A parametric sensitivity study of the physical models is given in Chapter 3.

The FEAST-METAL code is composed of several modules in coupled form to simulate metal fuel thermo-mechanical behavior, as listed in Table 2. The source code is written in FORTRAN-90 computing language.

The code implements an explicit numerical algorithm. The algorithmic flow chart is given in Figure 2. Note that the very high rate of creep strain of the fuel slug requires short time steps, of the order of 10-20 seconds. Therefore, a typical irradiation simulation requires use of about 106 time steps, resulting in an execution time of the order of minutes, when run on a single CPU personal computer.

The input file for the code allows specification of the operating conditions and initial fuel pin and coolant flow path geometry.

The code executes the following steps for each axial node at each time step:

- Radial power distribution within the fuel slug is calculated based on the actinide concentration within each radial node.
- Contact pressure between the fuel and clad is calculated as a function of displacement of fuel and cladding.
- The code calculates the fuel constituent redistribution, which is a relatively slow process, every 10000 seconds to reduce the computational time. Given the phase diagram and thermo-chemical activity of each phase, the code calculates the zirconium current and solves the diffusion equation by an explicit algorithm. Note that, both explicit and semi-implicit algorithms exist for this module. The semi-implicit algorithm could only be computationally efficient if one million second or higher time steps area selected. However, the rapid variation of the temperature distribution does not allow such large time steps; thus, an explicit algorithm is used for this module.
- Temperature distribution in the fuel pin is calculated as a function of radial power, zirconium, porosity distribution and sodium infiltration. The coolant axial temperature distribution is calculated with the Single Mass Velocity Model [19].

Consistently with the fuel constituent redistribution module, the calculation is performed every 10000 seconds. The Gauss-Seidel matrix solver algorithm is used [20].

- Having calculated the radial temperature distribution, the fuel stress/strain analysis is performed. Using the creep strains and axial strains calculated at the previous step, the average radial displacement can be calculated for each radial ring by using the Gauss-Jordan matrix solver algorithm [20]. After that, the axial force balance is used to calculate either the axial strain if the gap between the fuel and the clad is open; or, the fuel/clad friction force, if the gap between the fuel and the clad is closed. Finally, the creep and plasticity strains and open pore compressibility strain are calculated, which will be used in the next time step.
- Given the stress, temperature and fission rate of each radial ring, the fission gas release and swelling behavior of the fuel is calculated. Swelling due to diffusion of gas atoms into gas bubbles, coalescence of gas bubbles due to growth and bubble diffusion and open porosity formation have been accounted for. Moreover, an empirical relation is adopted for solid fission product swelling. No matrix solver is necessary in this module.
- Cladding wastage is calculated using the precipitation kinetics model.
- Given the contact pressure between fuel and cladding and coolant pressure outside the cladding, the radial displacement for each radial ring in the cladding are solved using the Gauss-Jordan matrix solver. After that, the axial force balance is used to calculate the axial strain. Finally, cladding creep strains are updated again and used in the next time step.
- Creep fracture margin of the clad is calculated by Cumulative Damage Fraction (CDF) and the constrained diffusional cavity growth models only for transients.
- The plenum pressure calculation is performed by assuming that the perfect gas law applies. The sum of the open porosity within the fuel slug and the plenum region at the top of the fuel slug constitutes the volume occupied by gas.

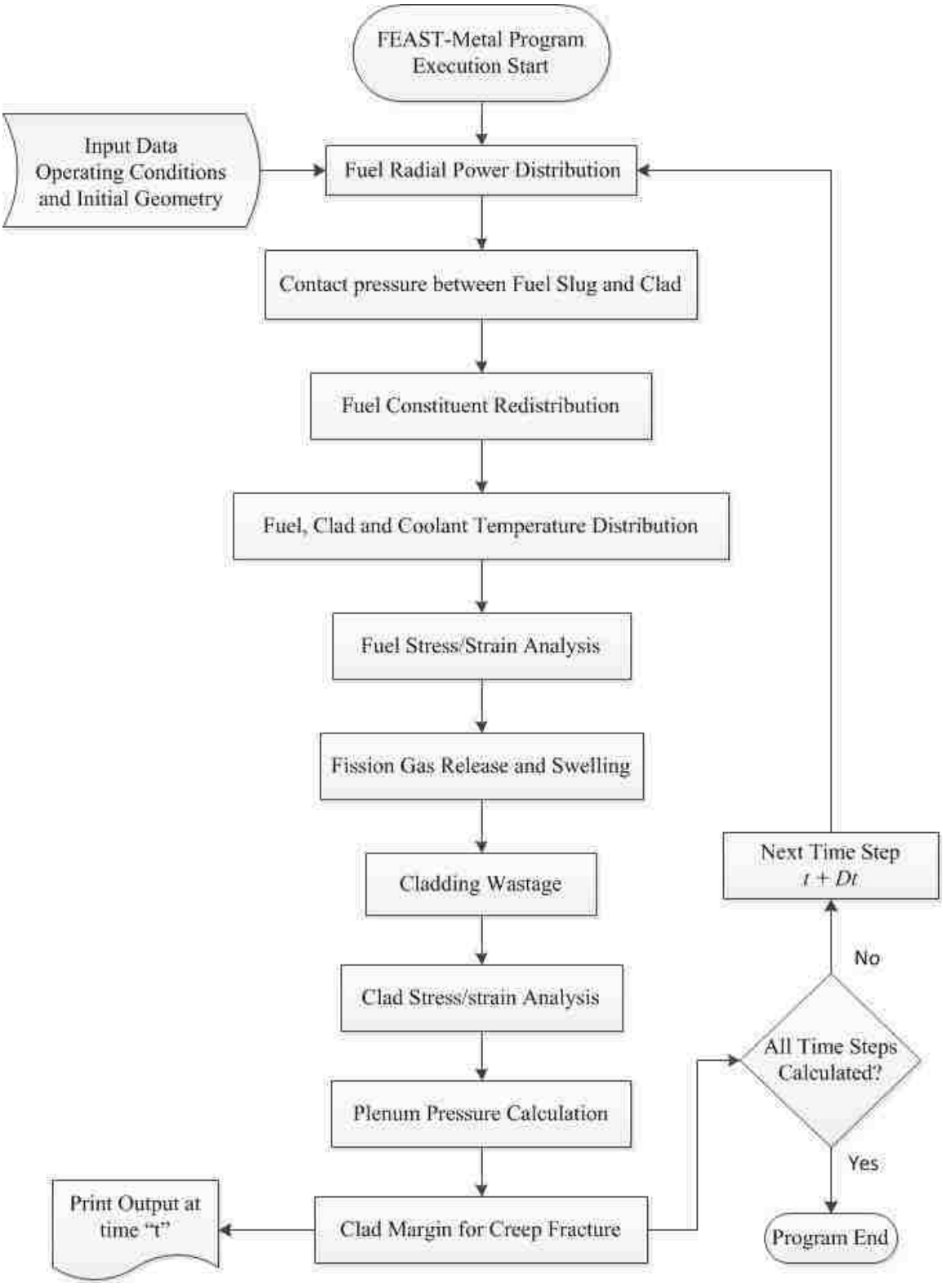

Figure 2. FEAST-Metal Code Flow chart

CHAPTER 3. FEAST-METAL PARAMETER SENSITIVITY STUDY

Purpose and Method

Important to the modeling and analysis work conducted with FEAST-Metal was the knowledge of, and the ability to calibrate, certain parameters within the code which are pertinent to the phenomena being modeled. In this way, we can reduce uncertainty in the results by benchmarking the FEAST-Metal code against known experimental data and correct any errors. The objective in this sensitivity study is to identify important macroscopic parameters of interest to modeling and simulation of metallic fuel performance. This enables one to calibrate on the correct parameters for the analysis to be performed.

In this study we applied advanced validation (sensitivity and uncertainty quantification) methods to the FEAST-Metal fuel performance code. This work supported later modeling and analysis which utilized some of the models adapted from FEAST. Our ultimate objective is to improve the models for adaptation and calibration after establishing an independent FEAST baseline.

We utilized an improved best estimate plus uncertainty methodology [4] which was previously used to perform calibration and sensitivity analysis of the LIFEIV code, as described in Reference 4. The sensitivity analysis provides identification of important macroscopic parameters of interest to modeling and simulation. Initially we identified a large number of parameters to consider in sensitivity analysis. Those parameters belonged to three categories. First, calibration parameters; those parameters have been identified by the code developers as the less well-defined-parameters in the fuel models and properties, and have been adjusted within physically realistic limits or measurement uncertainties to minimize the deviations between code results and fuel pin post-irradiation examination (PIE) data. The second set of parameters that were considered for the sensitivity study are input parameters to the code that include design (fabrication) parameters, operating conditions, and cladding and fuel properties. Lastly, the fuel and clad property models can play an important role in performance outputs. As a result of these large varieties of parameters we considered about 100 modeling parameters.

Six of the metallic fuel pins that were used in EBR-II experiments were selected for the sensitivity analysis. Fabrication and operational parameter ranges for those pins covered a significant portion of the complete set of EBR-II pins. Those pins also covered ranges of low and high burnups.

Our focus on the FEAST calculations was on the code calibration uncertainties, where a full sequence of screening and design code runs to support sensitivity analysis calculations were performed for a single metal fuel pin (T473 pin from the X425 experiment set) to test the sensitivity analysis methodology. This was followed by screening and design calculations that included all parameters of interest, namely the calibration, design, material properties, and operating parameters, where the calculations were performed for the T473 pin (the only pin for which we had sufficient experimental measured data to serve as reference output). Because of the large number of modeling parameters that needed to be obtained we decided to employ a screening methodology before conducting the detailed uncertainty analyses. This is because we have often observed in similar studies that ~80-90% of the variation in output can be accounted for by relatively few inputs, ~10-20%. Emulation of complex computer models often becomes substantially more difficult as input dimension increases; minimum inter-point distance increases, potentially having negative impact on covariance estimation. We found that resources are often used more efficiently with the two-stage procedure of screening followed by production analysis. Removal of inactive inputs results in (perhaps substantially) fewer computer model runs required for production analysis. Our approach in application of advanced validation to FEAST code assessment can be summarized as follows:

Phase I – Sensitivity screening

–Reduce number of parameters

Phase II – Sensitivity analyses with reduced parameter set

–Understand deficiencies in the modeling

–Determine modeling and experimental priorities

Table 4 provides a list of all 104 input parameters in FEAST-Metal. There are 20 design, operating and materials properties parameters and 84 calibration parameters and coefficients.

Table 4. Input parameters in FEAST-Metal: design, operating, and materials properties parameters (green) and calibration parameters (light blue).

	Calibration Parameters	
	Gas Release Model	
1	Gas release fraction coefficient 1	grf1
2	Gas release fraction coefficient 2	grf2
3	Fission yield of gas atoms	fyga
4	Fission density rate	fden
5	Transition probability bubble-i to bubble-i+1 (collision)	trprob
6	Bubble-1 nucleation constant	kb1nuc
7	Empirical bias factor for gas diffusion to closed bubble-1	egb1
8	Empirical bias factor for gas diffusion to closed bubble-2	egb2
9	Empirical bias factor for gas diffusion to open bubble-3	egb3
10	Gas Diffusion Factor	dgo
11	Gas activation energy for diffusion	gacten
12	Gas activation energy for surface diffusion	gactens
13	Radius of bubble-1	rb1
14	Radius of bubble-2	rb2
15	Surface diffusion coefficient	sdc
16	Empirical bias factor, diffusion to closed bubbles	ebb1
17	Empirical bias factor, diffusion to closed bubbles	ebb2
18	Empirical bias factor, diffusion to open bubbles	ebb3
19	Surface tension	st
20	Area occupied by surface molecule	ao
21	Threshold closed bubble swelling	sth
22	Fraction of interconnected bubbles at threshold swelling	fth
23	Correction factor for bubble volume after becoming open	fv
24	Correction factor for bubble area after becoming open	fs
25	Open bubble formation coefficient	d1
85	Plenum-to-Fuel Ratio	ptof
86	Fuel outer radius for each axial node (m)	rfo(i), i=1,im
87	Clad inner radius (m)	rci
88	Clad outer radius (m)	rco
89	Wire radius (m)	rw
90	Plutonium weight fraction	xpu
91	Zirconium weight fraction	xzr
92	Initial fill gas pressure (Pa)	fpgav
93	Bond sodium above the fuel level (m)	bonds
94	Fuel slug total length (m)	totl
95	Coolant pressure (Pa)	pco
96	Coolant inlet temperature (deg C)	tcin
97	Coolant outlet temperature ($^{\circ}$C)	tco(i), i=1,im
98	Clad Fast Flux to Dose Conversion Factor	dos
99	Plutonium fraction (at % per Heavy Metal)	pu425.txt
100	Power (W/m)	p425.txt
101	Total neutron flux (n/cm^2/s)	f425.txt
102	Fast flux fraction	fp425.txt
103	Fission density rate (fission/cm^3/s)	fi425.txt
104	Burnup (at %)	b425.txt

	Fuels - Phase Diagrams	
26	Enthalpy of solution coefficient 1	es1
27	Enthalpy of solution coefficient 2	es2
28	Creep Enhancement to Model Yield Stress enhp (4)	es3
29	Enthalpy of solution coefficient 4	es4
30	Effective heat of transport 1 (U-Pu-Zr, alpha)	eht1
31	Effective heat of transport 2 (U-Pu-Zr, delta)	eht2
32	Effective heat of transport 3 (U-Pu-Zr, beta)	eht3
33	Effective heat of transport 4 (U-Pu-Zr, gamma)	eht4
34	Diffusion coefficient for U-Zr alpha phase	doauzr
35	Diffusion coefficient for U-Zr delta phase	doduzr
36	Diffusion coefficient for U-Zr beta phase	dobuzr
37	Diffusion coefficient for U-Zr gamma phase	doguzr
38	Heat of transport for U-Zr alpha phase	qauzr
39	Heat of transport for U-Zr delta phase	qduzr
40	Heat of transport for U-Zr beta phase	qbuzr
41	Heat of transport for U-Zr gamma phase	qguzr
42	Multiplier for Diffusion coefficients for U-Pu-Zr alpha - delt	doauzrpu
43	First sodium corrosion rate coefficient	doduzrpu
44	Second sodium corrosion rate coefficient	dobuzrpu
45	Creep Constant mmm	doguzrpu
46	Creep Factor (qbarr)	qauzrpu
47	Creep Enhancement to Model Yield Stress enhp (1)	qduzrpu
48	Creep Enhancement to Model Yield Stress enhp (2)	qbuzrpu
49	Creep Enhancement to Model Yield Stress enhp (3)	qguzrpu
	Fuel properties	
50	Fuel thermal conductivity coefficient a	fka
51	Fuel thermal conductivity coefficient b	fkb
52	Fuel thermal conductivity coefficient c	fkc
53	Sodium infiltration coefficient	skfpc
54	Thermal conductivity liquid sodium	skon
55	Thermal conductivity HT9	qclad
56	Fuel specific heat (alpha + delta)	fcpad
57	Fuel specific heat (gamma phase)	fcpg
58	Fuel specific heat (beta + gamma)	fcpbg
59	transition temp (alpha+delta to beta+gamma)	ttem1
60	transition temp (beta+gamma to gamma)	ttem2
61	Specific heat HT9	ccp
62	Diffusion coefficient of beta atoms in alpha phase	da
63	Solubility limit of beta atoms in alpha phase	ca
64	Solubility limit of beta atoms in beta phase	cb
65	Concentration of the lanthanide atoms in the fuel	conl
66	Diffusion coefficient of lanthanides at fuel clad interface	qlandif
67	Solubility limit of the lanthanides in fuel	colca1
68	Solubility limit of the lanthanides in the clad	colcb1
69	Activation energy for lanthanide diffusion	ql
70	Diffusion constant for lanthanides	dol
71	Iron concentration within clad	cofe
72	Solubility limit for iron within $(U,Pu)_6Fe$ layer	cbfe
73	Solubility limit for iron within clad	café
74	Diffusion constant for iron	dofe
75	Activation energy for iron diffusion	qfe
76	Sodium corrosion rate	scor
77	Open porosity swelling strain contribution	eopn
78	Clad swelling strain	eclad
79	Fuel slug deformation anisotropy factor	fcrack
80	Grain boundary thickness	gbt
81	Grain boundary diffusion coefficient	dgbc
82	Dislocation Creep Constant (nnn)	ennn
83	Grain boundary free energy	gbfe
84	Free surface energy	fse

Table 5. Input parameters varied in Phase I of the sensitivity study

Parameter	Nominal	Uncertainty
grf1	0.8	20%
grf2	1.8	30%
fyga	0.3	10%
fden	5.50E+13	10%
trprob	1.0	50%
kb1nuc	1.00E-20	50%
egb1	1.0	50%
egb2	1.0	50%
egb3	1.0	50%
dgo	2.30E-03	50%
gacten	52000.0	50%
gactens	52000.0	50%
rb1	5.0E-07	50%
rb2	1.0E-05	50%
sdc	2.3	50%
ebb1	1.0	50%
ebb2	1.0	50%
ebb3	1.0	50%
st	0.8	50%
ao	9.00E-20	50%
sth	0.1	50%
fth	0.01	50%
fv	1.0	50%
fs	0.2	50%
d1	0.235	50%

Parameter	Nominal	Uncertainty
ptof	0.96	5%
rfo(i), i=1,im	0.00216	5%
rci	0.00254	5%
rco	0.00292	5%
rw	0.00071	5%
xpu	0.19	5%
xzr	0.1	5%
fpgav	84000	5%
bonds	0.00635	5%
totl	0.343	5%
pco	1.00E+05	5%
tcin	370	5%
tco(i), i=1,im	5, Min=477, Me	5%
dos	5	5%
pu425.txt	0.21	5%
p425.txt	2.90E+04	10%
f425.txt	1.90E+15	10%
b425.txt	9	10%

Parameter	Nominal	Uncertainty
es1	43764.5	50%
es2	-44174.7	50%
es3	30.0	50%
es4	38635.1	50%
eht1	200.0	50%
eht2	160.0	50%
eht3	450.0	50%
eht4	-150.0	50%
doauzr	2.00E-07	50%
doduzr	2.00E-07	50%
dobuzr	5.70E-05	50%
doguzr	1.54E-06	50%
qauzr	170.0	50%
qduzr	150.0	50%
qbuzr	180.0	50%
qguzr	119.04	50%
doauzrpu	1.00E+01	50%
doduzrpu	3.30E-06	50%
dobuzrpu	1.60E+04	50%
doguzrpu	1.00E+00	50%
qauzrpu	1.0	50%
qduzrpu	1000.0	50%
qbuzrpu	1.0	50%
qguzrpu	10000.00	50%

Parameter	Nominal	Uncertainty
fka	1.0	50%
fkb	1.0	50%
fkc	1.0	50%
skfpc	1.0	50%
skon	1.0	20%
qclad	1.0	50%
fcpad	1.0	50%
fcpg	1.0	50%
fcpbg	1.0	50%
ttem1	1.0	50%
ttem2	1.0	50%
ccp	1.0	50%
da	1.0	50%
ca	1.0	50%
cb	1.0	50%
conl	1.0	50%
qlandif	1.0	50%
colca1	0.0	50%
colcb1	0.1	50%
ql	300000.0	50%
dol	2300.0	50%
cofe	0.8	50%
cbfe	0.1	50%
café	0.0	50%
dofe	4.20E+06	50%
qfe	4.00E+05	50%
scor	1.0	50%
eopn	9.0	50%
eclad	1.0	50%
fcrack	0.68	20%
gbt	2.00E-05	50%
dgbc	1.10E-12	50%
ennn	5	50%
gbfe	0.85	50%
fse	2.1	50%

Gas Release Model
Fuels - Phase Diagrams
Fuel properties
Design & Operating Parameters

Phase I Screening Study Results

Variance-based global sensitivity analysis [5] was performed to screen for important parameters to include in probabilistic calibration and validation analysis with FEAST-Metal. Such screening is critical to reducing the computational burden imposed by model validation and assessment activities involving complex codes such as FEAST-Metal. Main and total effect sensitivity indices for all 100 parameters varied in this study were computed for 9 of the 11 calculated outputs considered from pin T473. Outputs CIW and CDF were not emulated well by the statistical techniques utilized to estimate the sensitivity indices. Results are presented in Table 6 for inputs associated with at least one output that exceeded a minimum sensitivity index threshold of 1%, chosen as the level at which any given input exceeds its performance under a scenario in which all inputs have equal effects (approximated by 100 percent divided by the total number of Phase I parameters). This threshold represents the level of sensitivity if all inputs were "equally active" in terms of inducing output variability.

Evaluated FEAST Output Parameter Definitions

Name	Description	Units
TFA	Fuel average temperature	°C
PFC	Contact pressure between fuel and clad in radial direction	MPa
CIW	Clad inner wastage	μm
COW	Clad outer wastage	μm
CRS	Total clad permanent hoop strain	%
PCT	Peak clad temperature	°C
FOR	Fuel outer radius for each axial node	m
TCL	Fuel centerline temperature	°C
CDF	Clad cumulative damage fraction	
FGR	Axial average for fission gas release	%
FUEL Δz	Average fuel axial elongation	%

Table 6. Main and total effect indices for nine outputs from pin T473. Indices exceeding the 1% sensitivity threshold are colored green, while inputs having an effect never exceeding 1% for any output are excluded (red).

MAIN EFFECTS									
Parameter	FGR (%)	Fuel Dz (%)	CRS (%)	PCT (deg C)	TCL (deg C)	TFA (deg C)	COW (mm)	PFC (MPa)	FOR (m)
gacten	95.25%	92.76%	78.88%	0.03%	0.15%	0.09%	0.00%	94.50%	37.74%
qduzr	0.00%	0.01%	0.01%	0.01%	5.12%	8.96%	0.00%	0.01%	0.01%
fkb	0.03%	0.05%	0.01%	0.01%	25.13%	20.40%	0.00%	0.05%	0.16%
skfpc	0.01%	0.01%	0.01%	0.01%	45.45%	29.98%	0.00%	0.01%	0.07%
kclad	0.01%	0.01%	0.01%	18.17%	0.65%	2.03%	0.00%	0.01%	0.01%
rfo	0.01%	0.01%	0.01%	0.01%	0.21%	0.24%	0.00%	0.01%	52.32%
rci	0.00%	0.02%	5.50%	6.81%	0.05%	0.17%	0.00%	0.01%	0.08%
rco	0.25%	0.04%	0.08%	7.60%	0.33%	0.84%	0.00%	0.52%	0.06%
bonds	0.00%	0.01%	1.93%	0.01%	0.03%	0.04%	0.00%	0.01%	0.01%
tcin	0.00%	0.01%	0.01%	20.50%	1.56%	3.88%	5.29%	0.01%	0.02%
tco	0.01%	0.01%	0.01%	43.51%	2.89%	7.25%	93.86%	0.03%	0.01%

TOTAL EFFECTS									
Parameter	FGR (%)	Fuel Dz (%)	CRS (%)	PCT (deg C)	TCL (deg C)	TFA (deg C)	COW (mm)	PFC (MPa)	FOR (m)
egb2	0.16%	0.16%	2.00%	0.02%	0.52%	0.64%	0.00%	0.04%	0.04%
gacten	97.66%	96.76%	90.23%	0.05%	0.71%	0.50%	0.01%	97.88%	44.25%
rb2	0.49%	1.16%	0.05%	0.02%	0.17%	0.29%	0.01%	0.12%	0.58%
doduzr	0.17%	0.62%	0.03%	0.02%	0.53%	1.02%	0.00%	0.03%	0.11%
qduzr	0.26%	0.23%	0.04%	0.02%	8.17%	15.86%	0.01%	0.03%	0.04%
fkb	0.38%	0.37%	0.04%	0.02%	29.84%	26.47%	0.00%	0.32%	0.37%
fkc	0.21%	0.11%	0.02%	0.02%	1.28%	0.93%	0.00%	0.02%	0.04%
skfpc	0.15%	0.19%	0.03%	0.02%	51.25%	35.65%	0.00%	0.04%	0.19%
kclad	0.22%	0.11%	0.04%	19.65%	1.29%	3.76%	0.00%	0.02%	0.06%
rfo	0.22%	0.20%	0.05%	0.03%	0.67%	0.82%	0.00%	0.03%	57.37%
rci	0.23%	0.17%	11.85%	7.42%	0.40%	1.48%	0.01%	0.03%	0.19%
rco	1.02%	0.27%	0.36%	8.34%	0.73%	1.87%	0.00%	1.54%	0.17%
bonds	0.17%	0.15%	4.70%	0.02%	0.20%	0.34%	0.00%	0.03%	0.04%
tcin	0.19%	0.14%	0.05%	20.85%	2.48%	5.94%	5.58%	0.03%	0.06%
tco	0.19%	0.16%	0.03%	44.02%	4.02%	9.72%	94.31%	0.09%	0.05%

Appendix A summarizes the technical details involved in computing main and total effect indices. Briefly, the main effect of a particular input is defined as the amount of output variance induced by uncertainty in that input after averaging out the (conditional) uncertainties in all other inputs. The main effect index is given by the ratio of this variance to the total output variance induced by the assumed uncertainties in all the inputs. Higher order effects due to uncertainties in two or more inputs, referred to as interaction effects, can also be estimated. The total effect variance of a particular input is the sum of its main effect and all interaction effect variances involving that input, with the total effect index computed by reference to the total output variance as described above for computing main effect indices. Therefore, the difference between total and main effects for a particular input provides an indication of the extent to which that input interacts with other inputs, which in turn indicates the degree of complexity in the input-output relationship.

We make the following observations:

- Input main effects often dominate variation in any given output.

- A small number of inputs are typically responsible for inducing most of the observed variation in any given output.

This screening exercise resulted in 32 parameters selected for a second phase of screening that involved output calculations from an additional 5 pins. Note that 15 outputs were identified in Table 6 as having significant total effects for at least one output. Nine of these were selected for the second phase: EGB2, GACTEN, RB2, DODUZR, QDUZR, FKB, FKC, SKFPC, and KCLAD. The additional six fuel design dimensional and operating parameters having significant total effects were not selected because they are viewed as being well-controlled and well-characterized with well-defined uncertainties: RFO, RCI, RCO, BONDS, TCIN, and TCO. Finally, 23 parameters from the gas release, phase diagram, and creep models were chosen for inclusion in the second phase due to their potential effects on diffusion coefficients and outputs: TRPROB, KB1NUC, EGB1, DGO, GACTENS, RB1, EBB1, EBB2, EBB3, ES1, ES2, ES3, ES4, EHT2, DOAUZRPU, DOGUZRPU, QAUZRPU, QDUZRPU, QBUZRPU, DGBC, ENNN, GBFE, and FSE.

PHASE II Sensitivity Analysis Results

Variance-based global sensitivity analysis was conducted to further screen the 32 input parameters identified in the first phase. This analysis was based on calculated outputs from pin T473 and five additional pins: DP04, DP11, DP21, DP45, and T452. The results based on total effect indices are shown in Table 7. For this analysis, the sensitivity threshold for selection was 3.125%. This is approximated by 100 percent divided by the total number of parameters analyzed in Phase II, which represents the level of sensitivity if all inputs were "equally active" in terms of inducing output variability. In other words, variables exceeding this level are contributing more than their "fair share", or exceeding their expected performance under a scenario in which all inputs have equal effects.

Table 7. Total effect sensitivity analysis results for six pins. Inputs exceeding the sensitivity threshold of 3.125% are colored green. Inputs never meeting the sensitivity threshold, and outputs not effectively emulated, are excluded.

	DP04	DP11		
Parameter	**PCT (deg C)**	**PCT (deg C)**	**TCL (deg C)**	**TFA (deg C)**
trprob	0.54%	0.44%	5.47%	2.16%
kb1nuc	0.48%	0.56%	2.79%	2.54%
egb1	0.53%	0.36%	2.01%	1.45%
dgo	0.72%	0.85%	2.10%	1.20%
gacten	2.16%	1.98%	10.16%	4.82%
rb1	0.34%	0.30%	2.43%	1.16%
rb2	0.55%	0.63%	2.79%	0.90%
ebb2	0.45%	0.50%	1.79%	2.85%
ebb3	0.55%	0.44%	2.82%	1.37%
es3	0.48%	0.42%	3.66%	1.42%
eht2	0.30%	0.48%	2.57%	1.41%
doduzr	0.26%	0.38%	2.15%	0.83%
qduzr	0.39%	0.38%	3.08%	1.63%
doauzrpu	0.44%	0.28%	4.17%	1.79%
qbuzrpu	0.42%	0.52%	2.06%	2.67%
fkb	0.44%	0.44%	4.27%	6.39%
fkc	0.54%	0.52%	2.39%	1.08%
skfpc	0.64%	0.35%	60.69%	54.29%
kclad	92.21%	92.64%	11.11%	29.34%
ennn	0.46%	0.26%	2.73%	1.70%
fse	0.57%	0.35%	3.56%	1.84%

	DP21							
	FGR (%)	Fuel Δz (%)	CRS (%)	PCT (deg C)	TCL (deg C)	TFA (deg C)	CIW (μm)	PFC (MPa)
trprob	0.37%	2.01%	2.88%	0.02%	0.12%	0.27%	1.27%	1.29%
kb1nuc	0.36%	3.02%	2.93%	0.02%	0.14%	0.19%	0.90%	3.28%
egb1	0.34%	1.13%	0.99%	0.01%	0.23%	0.18%	1.05%	0.90%
dgo	0.27%	1.67%	2.38%	0.02%	0.20%	0.20%	1.21%	6.53%
gacten	97.61%	77.65%	78.33%	0.05%	4.32%	3.46%	52.26%	80.18%
rb1	0.13%	0.85%	8.90%	0.02%	0.30%	0.16%	1.76%	2.51%
rb2	0.24%	2.13%	8.40%	0.02%	0.29%	0.53%	0.96%	10.08%
ebb2	0.14%	1.22%	1.76%	0.02%	0.14%	0.23%	1.01%	0.87%
ebb3	0.13%	0.77%	1.13%	0.02%	0.27%	0.33%	0.64%	0.97%
es3	0.20%	3.16%	1.73%	0.02%	0.10%	0.22%	0.62%	1.38%
eht2	0.13%	1.54%	0.95%	0.02%	0.09%	0.28%	1.25%	0.52%
doduzr	0.20%	3.35%	1.56%	0.02%	0.13%	0.19%	1.39%	0.81%
qduzr	0.16%	0.90%	1.47%	0.02%	0.14%	0.37%	1.54%	1.10%
doauzrpu	0.22%	1.15%	1.33%	0.04%	0.57%	0.59%	1.21%	0.95%
qbuzrpu	0.11%	9.06%	1.37%	0.03%	0.09%	0.53%	1.73%	1.99%
fkb	0.49%	5.85%	1.21%	0.03%	27.02%	23.35%	4.56%	1.44%
fkc	0.43%	0.94%	2.97%	0.02%	1.99%	1.62%	0.76%	2.26%
skfpc	0.58%	15.64%	3.86%	0.02%	65.66%	64.69%	2.36%	5.86%
kclad	0.53%	2.33%	1.14%	99.74%	1.38%	8.62%	50.31%	1.46%
ennn	0.25%	1.48%	2.46%	0.02%	0.15%	0.19%	2.08%	1.34%
fse	0.28%	1.40%	1.64%	0.02%	0.13%	0.30%	1.17%	2.39%

	DP45						
	FOR (m)	FGR (%)	PCT (deg C)	TCL (deg C)	TFA (deg C)	CIW (μm)	FOR (m)
trprob	0.16%	0.48%	0.28%	0.55%	0.95%	2.08%	1.10%
kb1nuc	0.25%	0.55%	0.35%	0.98%	0.77%	1.34%	1.53%
egb1	0.21%	0.43%	0.17%	0.40%	0.49%	1.78%	1.45%
dgo	0.85%	0.46%	0.26%	0.67%	0.74%	1.55%	1.35%
gacten	92.90%	96.23%	0.21%	0.94%	0.71%	52.88%	89.47%
rb1	1.39%	0.50%	0.22%	0.56%	0.42%	1.69%	1.44%
rb2	3.24%	0.41%	0.14%	0.52%	0.51%	1.87%	1.65%
ebb2	0.16%	0.35%	0.28%	0.23%	0.44%	1.45%	1.05%
ebb3	0.16%	0.59%	0.11%	0.28%	0.52%	1.66%	1.40%
es3	0.18%	0.39%	0.20%	1.09%	1.39%	3.35%	1.07%
eht2	0.19%	0.37%	0.17%	0.36%	0.39%	1.65%	1.26%
doduzr	0.16%	0.64%	0.17%	0.78%	0.53%	1.76%	1.37%
qduzr	0.23%	0.41%	0.11%	0.65%	0.48%	2.05%	0.97%
doauzrpu	0.28%	0.54%	0.16%	0.66%	0.51%	1.20%	1.43%
qbuzrpu	0.55%	0.38%	0.13%	0.66%	0.77%	1.04%	1.30%
fkb	1.16%	0.46%	0.16%	27.93%	25.94%	1.83%	2.40%
fkc	0.24%	0.37%	0.18%	2.33%	1.92%	2.26%	1.53%
skfpc	1.58%	0.45%	0.17%	62.45%	58.27%	1.74%	1.65%
kclad	1.77%	0.30%	97.19%	2.76%	12.09%	35.13%	2.45%
ennn	0.53%	0.38%	0.13%	0.57%	0.29%	0.86%	1.40%
fse	0.35%	0.46%	0.19%	0.55%	0.27%	1.15%	1.20%

	T452								
Parameter	FGR (%)	Fuel Δz (%)	CRS (%)	PCT (deg C)	TCL (deg C)	TFA (deg C)	CIW (μm)	PFC (MPa)	FOR (m)
trprob	0.49%	0.26%	2.96%	0.02%	0.12%	0.11%	0.89%	1.16%	0.56%
kb1nuc	0.21%	0.75%	1.15%	0.01%	0.10%	0.13%	1.42%	0.72%	0.20%
egb1	0.17%	0.18%	0.53%	0.01%	0.07%	0.10%	4.24%	0.29%	0.30%
dgo	0.31%	0.60%	2.17%	0.01%	0.09%	0.22%	2.11%	1.75%	0.71%
gacten	95.10%	95.06%	75.79%	0.02%	5.88%	2.03%	61.82%	87.39%	80.52%
rb1	1.64%	0.36%	4.40%	0.02%	0.33%	0.21%	31.44%	0.55%	2.00%
rb2	0.81%	1.53%	1.62%	0.01%	0.66%	0.46%	4.00%	0.53%	7.69%
ebb2	0.45%	4.42%	3.28%	0.01%	0.14%	0.14%	0.78%	0.95%	1.42%
ebb3	0.70%	0.49%	3.12%	0.01%	0.14%	0.17%	3.68%	3.43%	1.31%
es3	0.15%	0.22%	1.22%	0.02%	0.07%	0.07%	2.44%	0.28%	0.22%
eht2	0.57%	0.58%	1.58%	0.02%	0.13%	0.34%	3.63%	1.33%	4.72%
doduzr	0.97%	0.35%	4.26%	0.01%	0.14%	0.20%	4.42%	4.38%	2.14%
qduzr	0.15%	0.30%	2.38%	0.01%	1.69%	4.27%	11.63%	0.67%	0.61%
doauzrpu	0.24%	0.16%	1.88%	0.01%	0.16%	0.34%	2.85%	0.52%	0.92%
qbuzrpu	0.25%	0.35%	0.95%	0.01%	0.13%	0.08%	1.08%	0.25%	0.43%
fkb	0.26%	0.24%	0.98%	0.01%	15.23%	15.01%	1.19%	0.64%	1.52%
fkc	1.05%	0.41%	4.49%	0.01%	2.10%	1.89%	1.24%	2.05%	3.13%
skfpc	1.45%	3.23%	10.86%	0.01%	72.27%	62.98%	1.19%	3.66%	3.84%
kclad	1.12%	0.40%	5.78%	99.87%	3.75%	14.82%	25.66%	0.60%	0.58%
ennn	0.58%	0.68%	6.17%	0.01%	0.10%	0.10%	1.01%	3.73%	2.59%
fse	0.31%	0.15%	0.99%	0.01%	0.08%	0.10%	2.10%	0.94%	0.58%

T473				
	FGR (%)	CRS (%)	PFC (MPa)	FOR (m)
trprob	0.06%	0.12%	0.13%	1.43%
kb1nuc	0.89%	1.19%	2.82%	0.34%
egb1	0.18%	0.30%	0.44%	1.06%
dgo	0.34%	0.39%	0.60%	4.02%
gacten	98.99%	90.88%	94.28%	92.56%
rb1	0.25%	5.37%	2.13%	2.69%
rb2	0.19%	11.55%	6.10%	4.63%
ebb2	0.08%	0.19%	0.24%	0.13%
ebb3	0.09%	0.46%	0.35%	0.25%
es3	0.05%	0.14%	0.12%	0.24%
eht2	0.04%	0.65%	0.39%	0.57%
doduzr	0.40%	0.27%	0.69%	0.28%
qduzr	0.48%	3.47%	3.65%	2.61%
doauzrpu	0.04%	0.11%	0.08%	0.11%
qbuzrpu	0.19%	0.15%	0.12%	0.28%
fkb	0.39%	0.60%	1.55%	1.74%
fkc	0.02%	0.19%	0.97%	0.34%
skfpc	0.84%	3.55%	5.85%	4.69%
kclad	0.12%	1.44%	1.64%	2.58%
ennn	0.04%	0.15%	0.23%	0.20%
fse	0.02%	0.10%	0.08%	0.38%

Of the 21 parameters with significant total effects, only 8 had significant main effects (as shown in Tables 7 and 8): GACTEN, RB1, RB2, QDUZR, QBUZRPU, FKB, SKFPC, and KCLAD. Statistical estimates of main effects are the most reliable due to their simplicity relative to interaction effects, suggesting these 8 parameters should be deemed significant with the highest confidence. The additional 13 parameters of Table 3 are serious contenders for retention due to their possible interaction with other parameters: TRPROB, KB1NUC, EGB1, DGO, EBB2, EBB3, ES3, EHT2, DODUZR, DOAUZRPU, FKC, ENNN, and FSE. Finally, 11 of the original 32 parameters considered in this phase never met the sensitivity threshold for any of the outputs considered across all six pins: EGB2, GACTENS, EBB1, ES1, ES2, ES4, DOGUZRPU, QAUZRPU, QDUZRPU, DGBC, and GBFE (see Table 9).

Table 8. Recommended modeling parameters: Eight most important ones with high confidence are red colored parameters, 13 blue colored parameters should be kept in the list until confidence to eliminate or keep them is increased with further studies.

	Gas Release Model
gacten	Gas activation energy for diffusion
rb1	Radius of bubble-1
rb2	Radius of bubble-2
trprob	Transition probability bubble-i to bubble-i+1 (collision)
kb1nuc	Bubble-1 nucleation constant
egb1	Empirical bias factor for gas diffusion to closed bubble-1
dgo	Gas Diffusion Factor
ebb2	Empirical bias factor, diffusion to closed bubbles
ebb3	Empirical bias factor, diffusion to open bubbles
	Species Diffusion Model
qduzr	Heat of transport for U-Zr delta phase
eht2	Effective heat of transport 2 (U-Pu-Zr, delta)
doduzr	Diffusion coefficient for U-Zr delta phase
doauzrpu	Multiplier for Diffusion coefficients for U-Pu-Zr alpha - delta - beta phases
	Fuel Creep Model
qbuzrpu	Creep Enhancement to Model Yield Stress enhp (2)
es3	Creep Enhancement to Model Yield Stress enhp (3)
	Thermal Properties
fkb	Fuel thermal conductivity coefficient b
skfpc	Sodium infiltration coefficient
kclad	Thermal conductivity HT9
fkc	Fuel thermal conductivity coefficient c
	Others
ennn	Dislocation Creep Constant (nnn)
fse	Free surface energy

Out of this recommended set of parameters, of most interest to this study are the Species Diffusion Model parameters (qduzr, eht2, doduzr, doauzrpu). In particular, it is the Heat of Transport for the U-Zr delta phase (qduzr) which is most useful for the analysis to follow.

Table 9. Parameters found not meeting sensitivity threshold; therefore they will not be considered in future optimization.

	Gas Release Model
gactens	Gas activation energy for surface diffusion
egb2	Empirical bias factor for gas diffusion to closed bubble-2
ebb1	Empirical bias factor, diffusion to closed bubbles
	Species Diffusion Model
es1	Enthalpy of solution coefficient 1
es2	Enthalpy of solution coefficient 2
es4	Enthalpy of solution coefficient 4
	Fuel Creep Model
doguzrpu	Creep Constant mmm
qauzrpu	Creep Factor (qbarr)
qduzrpu	Creep Enhancement to Model Yield Stress enhp (1)
	Others
dgbc	Grain boundary diffusion coefficient
gbfe	Grain boundary free energy

Manual Verification of Main Effects

In Phase II, we noted some unexpected results:

- Gas release model parameters (gacten, rb1, rb2) showed a significant effect on CIW, COW.

Steady state clad wastage is dependent only on a diffusion coefficient, and ultimately temperature, according to [1]:

Steady state clad wastage prediction with precipitation kinetics model is given as follows:

$$\frac{dX_w}{dt} = \frac{1}{2}\frac{C_{oL} - C_{\alpha L}}{C_{\beta L} - C_{\alpha L}}\sqrt{\frac{D_L}{t}}$$

X_w : Clad wastage layer thickness (m)

C_{oL} : Concentration of the lanthanide atoms in the fuel

$C_{\alpha L}$: Solubility limit of the lanhanides in the fuel (zero)

$C_{\beta L}$: Solubility limit of the lanthanides in the clad (0.1)

D_L : Diffusion coefficient of lanthanides at fuel clad interface (m^2/s)

t: Time (sec)

Lanthanide diffusion coefficient is given with following relation.

$$D_L = D_{0L}\exp(-\frac{Q_L}{RT})$$

To explore this apparent anomaly, we performed the following study:

- We ran several cases on DP21, changing gacten by 20% to 60%. We encountered a threshold value, somewhere around 25% increase in gacten, above which results in all zero values for CIW on output. (We had experienced this in an earlier stage, but we did not know where the threshold value was.)
- With 20% increase in gacten, there is virtually no change in COW. All the change appears to be in CIW (inner wastage). There is a significant increase in CIW with an increase in gacten.
- Examined temperature variation. While the fuel centerline temperature increases around the axial midpoint nodes of the pin, it shows a slight decrease toward the ends. Fuel average temperatures show a slight drop for the length of the pin.

$$D_L = D_{0L}\exp(-\frac{Q_L}{RT})$$

DP21 reference:

- Last temp at highest point = 655 C

  exp(-300000/(8.314 (655+273))) = 1.3e-17

inner wastage = 22.6

DP21 high gacten:

- Last temp at highest point = 645 C

  exp(-300000/(8.314 (645+273))) = 8.5e-18

  inner wastage = 25.8

High gacten reduces the temperature and diffusion coefficient. According to the equation for clad wastage thickness growth rate, we should expect dx/dt to go down and therefore see less wastage thickness. However, wasi1 output (last row last number) shows it is increasing. A possible error may exist in the FEAST code models. This warrants further investigation, outside the scope of this study.

Manual bubble radius test results are as follows:

- Rb1 large: significant increase in CIW, slight increase in COW.
- Rb1 small: run termination, but with earlier and rapid increase in CIW. Slight increase in COW.
- Rb2 large: significant increase in CIW, slight increase in COW.
- Rb2 small: early run termination, but with earlier and rapid increase in CIW. Slight increase in COW.

The results obtained (with varying rb1, rb2) are a larger effect on inner wastage, with little or no effect on outer wastage. It is unclear as to why the sensitivity analysis shows such a significant effect on clad outer wastage (COW). This is not evident in the FEAST output.

Summary and Recommendations

We have completed an initial sensitivity study to reduce the dimensionality of the input parameter space studied in this work. The parameters used can be classified in three main categories: (a) design parameters such as power, fuel dimensions, etc., controlled by other calculations or manufacturing, (b) modeling parameters such as specific heat of fuel where there is a reasonable model with limited empiricism, and (c) calibration parameters

adjusted by code developers to predict experimental data (adjustable constants in key models). Two phases of this study were conducted. First we performed a screening study on an EBR-II metal fuel pin, to reduce the number of significant parameters from about 100 down to 32. We then ran cases on the first pin and 5 additional pins to target the reduced parameter set, and performed a more thorough sensitivity analysis to find the most significant parameters and most sensitive models.

The fuel thermal conductivity and gas release models were most influential in terms of explaining overall output variability, and are therefore targets for additional calibration to further constrain their parameters. We considered all results to recommend a ranking of models that can be considered for further improvements. Our model ranking is as follows:

- Fission gas release and swelling,
- Fuel and clad conductivity,
- Species diffusion, and
- Fuel creep.

We identified several input parameters in the FEAST-Metal code which have a significant impact on key outputs.

Sensitivity analysis may generate unexpected results that require manual verification.

It remains unclear why the analysis indicates a significant effect on clad outer wastage with varying gas activation energy (gacten). We expect the more significant effect on inner wastage, but not on COW.

Formal methods of variable selection are difficult to apply in the FEAST-Metal setting due to the computational burden.

We will consider analyzing false positive/negative rates of the simple method applied in this study.

The final list of parameters for follow-on calibration studies is as follows:

- gacten, rb1, rb2, fkb, skfpc, kclad.

Our ultimate goal is to validate calibrated parameter distributions for use in implementing improvements to the fission gas release, fuel conductivity, and species diffusion models from FEAST-Metal. To that end, we recommend performing parameter calibration and validation on the models of interest, using additional validation data. Improved models can then be implemented in Bison-Metal in the future, when that tool is fully developed.

We have identified the calibration parameters of most interest to this study; namely, the Species Diffusion Model parameters (qduzr, eht2, doduzr, doauzrpu). In particular, it is the Heat of Transport for the U-Zr delta phase (qduzr) which is most useful for the analysis to follow.

CHAPTER 4. FEAST-METAL CONSTITUENT REDISTRIBUTION MODEL

Modeling of Constituent Redistribution in U-Zr and U-Pu-Zr fuel

Fuel constituent migration, which has been observed in irradiated metallic fuel, affects the fuel slug material properties such as solidus and liquidus temperatures, thermal conductivity, mechanical properties such as modulus of elasticity, fuel cladding eutectic reaction rate, and radial power density profile, particularly in enriched uranium alloy fuels. Thus, modeling of constituent redistribution is essential when developing a metallic fuel performance code. Upon constituent redistribution the microstructure of irradiated metal fuel exhibits three distinct concentric zones: a zirconium-enriched central zone, a zirconium-depleted and uranium-enriched intermediate zone, and a zirconium-enriched zone on the outer periphery. The migration of zirconium atoms is driven by the chemical activity gradients that develop within the fuel when the radial temperature distribution creates multiple crystalline phases of the fuel alloy.

Major Assumptions

The model given by Kim in [8] is implemented in the FEAST-METAL code. It is based on thermo-transport theory. The following assumptions are adopted from [8] and [9].

1. Local equilibrium assumption. Phase changes (determined by a change in local concentration and/or temperature) are assumed to occur very rapidly compared with the migration of alloy constituents.
2. Pu does not migrate; hence, the U and Zr concentration profiles are proportionally opposite each other.
3. The equilibrium phases of the ternary U-Zr-Pu system are described by using a quasi-binary U-Zr phase diagram (with constant Plutonium content), which is produced from ternary phase diagrams, assuming uniformity of Plutonium in each phase of the multiphase zones.
4. The minimum allowed Zirconium concentration in the Zirconium depleted middle region is 5 at % due to the solubility limit. When the concentration of a radial node drops below 5 at%, further diffusion from this node to the adjacent nodes is

not allowed. This limit corresponds to depletion of the matrix phase in the middle region.

5. The cross-terms, relating the flux of one species to the chemical potential gradient of another species, in the constitutive equations are negligible.
6. The presence of plutonium in the alloy at levels greater than 8 wt% enhances uranium and zirconium migration by an order of magnitude.
7. Only radial migration of zirconium is considered. Axial temperature gradients are relatively small and axial zirconium redistribution has not been observed experimentally.
8. The radial power distribution in the fuel slug is assumed to be directly proportional to the actinide concentration distribution.

The plutonium uniformity assumption is partly justified on the basis of the following observations from Ref. [9]:

1. Plutonium shows relatively large miscibility in various phases of the system in the operating temperature range.
2. Irradiation data of the ternary system show that redistribution of plutonium is minimal.
3. Theoretical calculations show that the equilibrium tie lines in the vicinity of the ternary fuel compositions of interest run approximately parallel to the constant plutonium line in the isothermal sections of the U-Pu-Zr ternary phase diagram for the operating temperature range.

Fundamental Data

The phase diagrams, diffusion coefficients and effective heats of transport of zirconium and uranium in the ternary alloy are the fundamental data required in this model.

Phase Diagrams:

The thermochemical driving force for constituent migration is determined by the various phases present in the fuel at the operating temperatures, an accurate estimate of the phase diagram is essential to the development of the fuel restructuring model. Assuming a fixed Pu concentration of 19 wt %, a simplified pseudo-binary phase diagram

was developed for U-Pu-Zr alloys [8], which is based on the available ternary phase diagrams for the temperatures of interest. The U-Zr phase diagram is given in Ref. [11]. Figure 3 shows a generic pseudo-binary phase diagram for U-Pu-Zr alloys. The solubility lines 1 through 6 are linearly interpolated between U-Zr and U-19Pu-Zr fuels, and are given as functions of temperature in Table 10. This approach is adopted to examine the fuel for varying plutonium contents (0-26 wt %). Note that, similar approaches are recommended in Ref. [8] and [9].

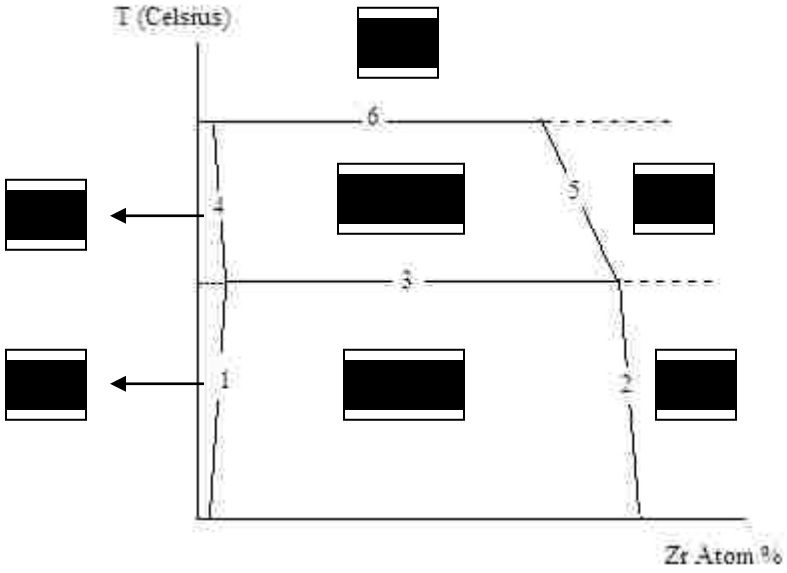

Figure 3. Pseudo binary phase diagram for U-Pu-Zr Fuel for fixed Pu content [8]

Table 10. Solubility Lines

Solubility line	U–Zr	U–19Pu–Zr
1	$x_{Zr} = 0.01$	$x_{Zr} = 0.001 + (T - 773.15)/2968.8$
2	$x_{Zr} = \frac{T-813.15}{935.15-813.15} \times (0.588 - 0.676) + 0.676$	$x_{Zr} = 0.539 - \frac{T-773.15}{9500.0}$
3	$T = 935.15$	$T = 868.15$
4	$x_{Zr} = 0.01$	$x_{Zr} = 0.032 - \frac{T-868.15}{6111.1}$
5	$x_{Zr} = \frac{T-935.15}{965.15-935.15}(0.444 - 0.588) + 0.588$	$x_{Zr} = 0.529 - \frac{T-868.15}{440.5}$ $T < 905$, $x_{Zr} = 0.445 - \frac{T-905.15}{200}$ $T \geqslant 905$
6	$T = 965.15$	$T = 923.15$

x_{Zr}: Zirconium molar fraction.
T: Temperature (K).

Enthalpy of Solution:

The enthalpy of solution of Zirconium in α and β phases is negligible [11]. On the other hand, the enthalpy of solution of the γ and δ matrix phases are given in [8] as follows:

$$\Delta\bar{H}_s = G_{Zr}^{\bar{E}} - T\frac{\partial G_{Zr}^{E}}{\partial T}$$

$$G_{Zr}^{\bar{E}} = x_U^2\left(43764.5 - 22T - 44174.7x_{Zr} + 38635.1x_{Zr}^2\right)$$
$$+x_{Pu}^2\left(6574.7\right) + x_U x_{Pu}\left(15884\right)$$

$\Delta\bar{H}_s$: Enthalpy of solution (J/mol)
G_{Zr}^{E} : Free energy of Zirconium (J/mol)
x_U : Uranium mole fraction
x_{Zr} : Zirconium mole fraction
x_{Pu} : Plutonium mole fraction
T : Temperature (K)

Effective Heat of Transport:

The heats of transport for each phase field were obtained by a best fit in Ref. [8] and Ref. [12] to reproduce the measured redistribution profile of U-Pu-Zr and U-Zr fuels, respectively. The results are given in Table 11.

Table 11. Effective heat of transport (kJ/mol)

Phase	U->8Pu-Zr	U-Zr
α	200	0.0
δ	160	0.0
β	450	0.0
γ	−200	-150

Note that the effective heat of transport values are linearly interpolated between their values for the U-Zr and U-8Pu-Zr alloys. For plutonium concentrations above 8 wt %, it is assumed that the effective heat of transport values stay constant.

The negative heat of transport in the γ phase generates the driving force for zirconium to

migrate towards the center (hotter) region of the fuel slug, even after zirconium accumulation in the center region creates an opposing concentration gradient. The positive heats of transport for the α, β and δ phases let zirconium migrate toward the fuel surface.

Effective Interdiffusion Coefficients:

The interdiffusion coefficient of Zirconium for U-Pu-Zr is not available. Therefore it was estimated to best fit the experimental data in Ref. [8].

The influence of plutonium addition and irradiation on the zirconium migration kinetics is handled by some enhancement factors. The existence of plutonium in a ternary fuel has been assumed to increase the interdiffusion coefficient [8], and the diffusion coefficients for each phase have been found by matching the experimental data for the T-179 fuel rod [8]. The results are given in Table 12 for the U-Zr alloy [11] and Table 13 for the U-Pu-Zr alloy with Plutonium weight fraction greater than 0.08. The gamma phase diffusion coefficient given in Ref. [11] depends on the zirconium molar fraction. Note that the quadratic dependency of the diffusion coefficient on the zirconium mole fraction is preserved for both U-Zr and U-Pu-Zr fuels.

Table 12. Diffusion coefficients for U-Zr alloy phases

Phases	D_o (m²/s)	Q (kJ/mol)
α	2×10^{-7}	170
δ	2×10^{-7}	150
β	5.7×10^{-5}	180
γ	$10^{(-5.1-8.05x_{Zr}+9.13x_{Zr}^2)}$	$128-107x_{Zr}+174x_{Zr}^2$

Table 13. Diffusion coefficients for U-Pu-Zr alloy phases (Pu is > 8 wt %)

Phases	D_o (m²/s)	Q (kJ/mol)
α	2×10^{-6}	170
δ	2×10^{-6}	150
β	4.0×10^{-4}	180
γ	$10^{(-5.1-8.05x_{Zr}+9.13x_{Zr}^2)}$	$128-107x_{Zr}+174x_{Zr}^2$

The Zr diffusion coefficient for the dual phase β + γ is calculated by the diffusion coefficient of the β and γ phases from Table 13 multiplied by a factor of 10 depending on whether the β or γ phases exceed 50 %, respectively.

Model Development:

The one dimensional continuity equation for zirconium can be expressed in cylindrical coordinates as follows:

$$\frac{\partial C_{Zr}}{\partial t} = -\frac{1}{r}\frac{\partial (rJ_{Zr})}{\partial r} + s$$

C_{Zr}: Zirconium concentration (atom/m³)

J_{Zr}: Interdiffusion flux (atom/m²/s)

s: Zirconium production rate by fission. The Zirconium yield is 0.2 for the fission of Plutonium

Within a single γ phase field the zirconium interdiffusion flux is given by

$$J_{Zr} = -D_{Zr}^{\gamma}\left(\frac{\partial C_{Zr}}{\partial r} + \frac{Q_{Zr}C_{Zr}}{RT^2}\frac{\partial T}{\partial r}\right)$$

D_{Zr}^{γ}: Effective interdiffusion coefficient of zirconium in γ phase (m²/s)

Q_{Zr}: Heat of transport of zirconium in γ phase (J/mol)

R: Gas constant (8.314 J/mol/K)

T: Local fuel temperature (K)

When the concentration gradient becomes equal to the chemical potential gradient, the diffusion in the γ phase inherently stops.

Within a dual phase field such as α + δ and β + γ, the driving force for diffusion is affected by the solubility of zirconium in the precipitation phases.

$$J_{Zr} = -V_1 D_{Zr,1}^{eff} C_{Zr,1} \frac{\Delta \bar{H}_{i,1} + Q_{Zr,1}}{RT^2} \frac{\partial T}{\partial r} - V_2 D_{Zr,2}^{eff} C_{Zr,2} \frac{\Delta \bar{H}_{i,2} + Q_{Zr,2}}{RT^2} \frac{\partial T}{\partial r}$$

V_1: Volume fraction of a phase-1

Note that subscript "1" represents the first phase and subscript "2" represents the second phase.

Discretization of the radial continuity equation results in

$$C_{Zr}^{t} = C_{Zr}^{t} + 2\Delta t \frac{J_{-}^{i-1} \times rc^{i-1} - J_{-}^{i} \times rc^{i} + J_{+}^{i} \times rc^{i} - J_{+}^{i+1} \times rc^{i+1}}{(r^{i})^2 - (r^{i-1})^2} + s\Delta t$$

rc^i: Weight center of the radial node-i (m)

r^i: Outer boundary of node-i (m)

J_+^i: Positive zirconium current emerging from node-i towards outer part of the fuel. Its sign is positive (atom/m²/s)

J_-^i: Negative zirconium current emerging from node-i towards inner part of the fuel. Its sign is negative (atom/m²/s)

s: Zirconium production rate (atom/m³/s)

Δt: Time step (sec)

The equation for zirconium interdiffusion flux is solved explicitly for each fuel axial node.

Boundary Conditions

The boundary conditions are that the negative current at the origin of the fuel slug as well as the positive current at the surface of the fuel slug are zero, as follows:

at r=0.0 $J_-^i = 0.0$

at r=R $J_+^i = 0.0$ (Zirconium cannot migrate out of the fuel)

Modification for AFC Fuels with Higher Zr and Pu Content

In the following chapter, we will focus on the constituent and actinide migration modeling and analysis results. In order to perform this modeling and analysis using

FEAST-Metal, it was necessary to modify the source code and re-compile it with recalculated parameters to obtain the output data required for this study. The data of interest are not included as output in the released version of the code. Additionally, the first release of the code was unable to successfully calculate the outputs of interest for high-zirconium or high-plutonium content fuels. Thermal conductivity of high zirconium and high plutonium content fuels are not available. Instead, it was necessary to employ approximate relations. The following thermal conductivity relations for U–Zr and Pu–Zr binary alloys were adopted as described in Ref. [23]:

$$k_{U-Zr} = \left(1 - \sqrt{(1 - x_{Zr})}\right) \times k_{Zr} + \sqrt{(1 - x_{Zr})}(x_{Zr} k_{c,U} + (1 - x_{Zr}) \times k_U)$$

$$k_{Pu-Zr} = \left(1 - \sqrt{(1 - x_{Pu})}\right) \times k_{Pu} + \sqrt{(1 - x_{Pu})} \times k_{c,Zr}$$

$$k_U = 21.73 + 1.591 \times 10^{-2} T + 5.907 \times 10^{-6} T^2$$

$$k_{Zr} = 8.853 + 7.082 \times 10^{-3} T + 2.533 \times 10^{-6} T^2 + 2.992 \times 10^{3} T^{-1}$$

$$k_{Pu} = 3.225 + 0.0296T \text{ (δ-Pu phase)}$$

$$k_{c,U} = -102 + 200.1 x_{Zr} - 109.2 x_{Zr}^2 + 9.435 \times 10^{-3} T + 3.459 \times 10^{-5} T^2 - 0.02093 x_{Zr} T$$

$$k_{c,Zr} = 29.469 - 118.811 x_{Pu} + 88.893 x_{Pu}^2 - 0.0117T + 1.922 \times 10^{-5} T^2 - 0.00716 x_{Pu} T$$

Here, k_{U-Zr} is the uranium zirconium mixture thermal conductivity (W/m/K), k_{Pu-Zr} is plutonium zirconium mixture thermal conductivity (W/m/K), k_U is uranium thermal conductivity (W/m/K), k_{Pu} is δ phase plutonium thermal conductivity (W/m/K), $k_{c,U}$ is the thermal conductivity correction due to alloying effect for U–Zr, $k_{c,Zr}$ is the thermal conductivity correction due to the alloying effect for Pu–Zr, x_{Zr} is zirconium weight fraction, x_{Pu} is plutonium weight fraction, and T is the temperature (K).

Because the AFC fuel operates around the γ and δ solubility limits (see Fig. 3), complete miscibility of the fuel constituents is assumed in order to approximate the

thermal conductivity of the U–Pu–Zr ternary alloy. For a given alloy of aU–bPu–cZr, where a, b, and c are weight fractions, the thermal conductivity of aU–cZr and bPu–cZr binary alloys are calculated (after doing the normalization) using the first two equations from [23]. Then, average thermal conductivity of the aU–bPu–cZr ternary alloy is calculated by weight averaging the binary alloy thermal conductivities as follows:

$$k_{\mathrm{U-Pu-Zr}} = \frac{a}{a+b} k_{\mathrm{U-Zr}} + \frac{b}{a+b} k_{\mathrm{Pu-Zr}}$$

Note that the U–Zr and Pu–Zr thermal conductivities in the two first equations are close to each other for a wide range. Therefore, sensitivity of overall results on the weight averaging procedure is low. Higher fidelity approaches to assess thermal conductivity of the ternary system can be adopted.

This re-calculation of thermal conductivity was necessitated by the fact that the unmodified FEAST-Metal code would fail on "temperature out of range" with inputs for high-Zr or high-Pu fuel.

Limitations and Restrictions on This Work

The challenges posed by the relative scarcity and lack of availability of experimental data cannot be denied when evaluating the results obtained. The PIE data from AFC fuels is unpublished as of this writing and may not be shared here explicitly. EBR-II data from 20 to 30 years ago is still difficult to extract from ANL. Nonetheless, the results of this study (as presented in the following chapter) agree quite well with the experimental results that could be collected.

CHAPTER 5. RESULTS

Constituent redistribution in two of the EBR-II fuel pins was modeled and observed, in order to confirm the results previously obtained by Karahan [1]. Two of the AFC rodlets from the AFC-1D test assembly (1DR1) and AFC-1F were also modeled for comparison of the experimental results with FEAST-Metal results.

EBR-II Results

Figure 4 depicts three sets of results, showing the EBR-II typical experimental data, along with FEAST results by Karahan [1] and those of the Kim [8] model. Zirconium migration is evident in all three sets of data, and they all agree quite well.

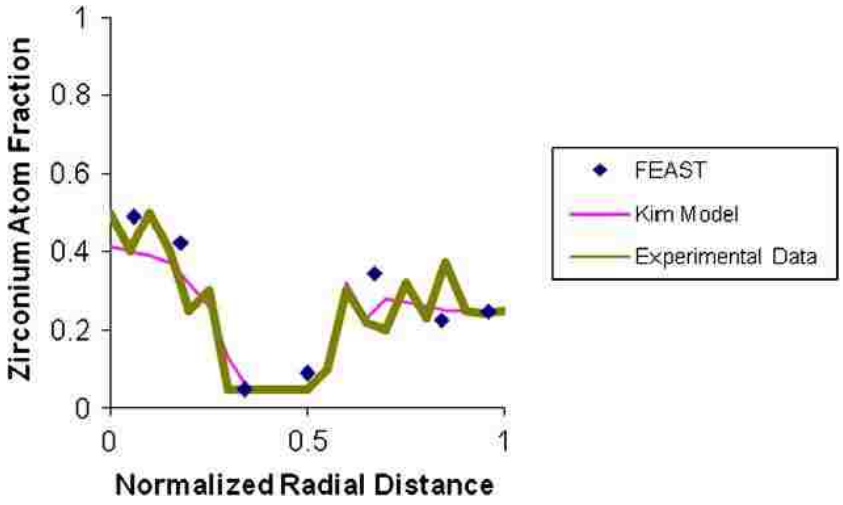

Figure 4. EBR-II Zirconium Atom Fraction

In Figure 5, we see the confirmatory results from this study, after calibration and modeling with the modified FEAST code. Results are from the EBR-II T473 test pin from the X425 test set, and agree well with the example comparison in the previous figure.

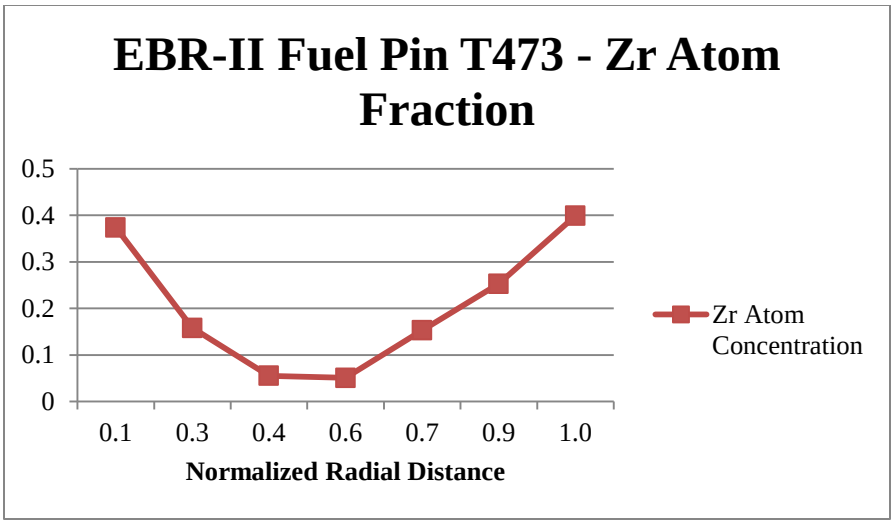

Figure 5. EBR-II Fuel Pin T473 Zr Atom Fraction

In Figure 6, another EBR II fuel pin, the T179 pin, is the same one depicted in the earlier Figure 5. Here we demonstrate that our calibration is good, because the zirconium redistribution is very much aligned with the experimental and other analytical results.

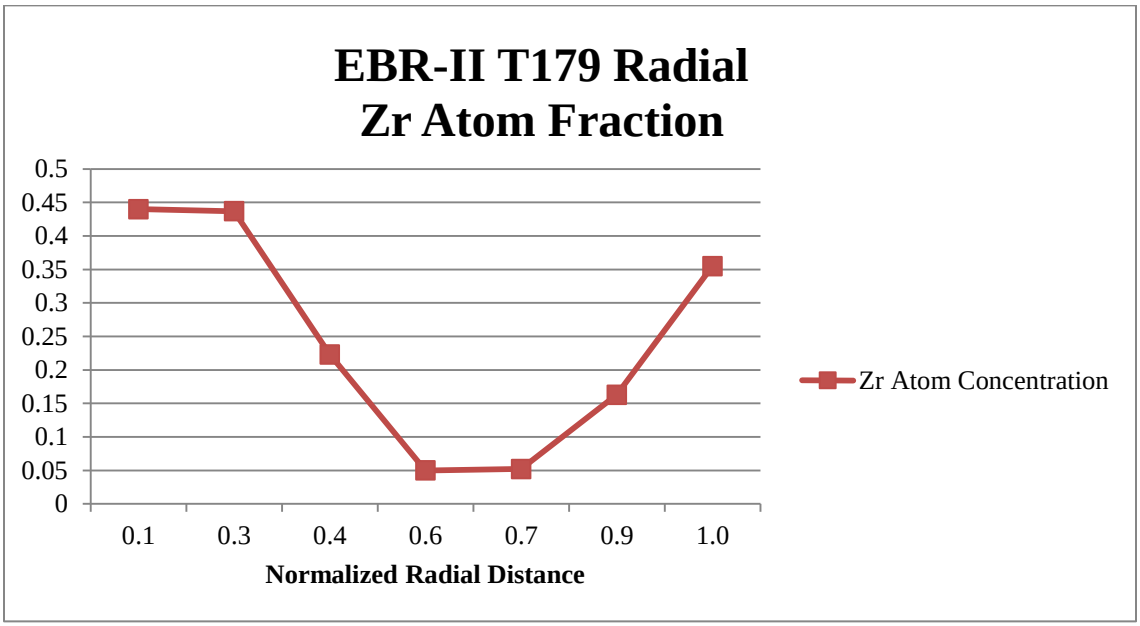

Figure 6. EBR-II T179 Zr Atom Fraction

AFC Results

Figure 7 illustrates the typical AFC fuel rodlet geometry.

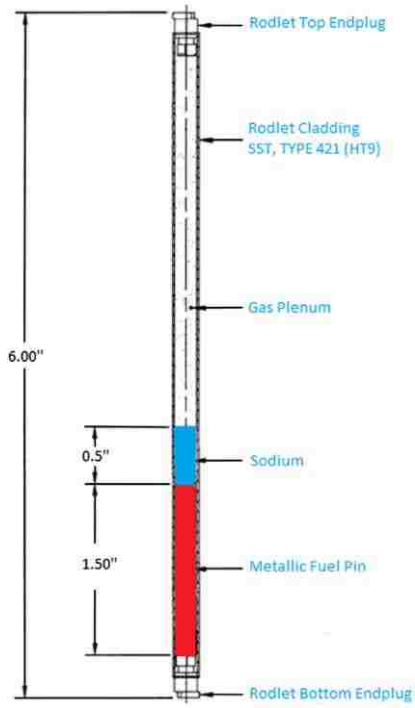

Figure 7. Typical geometry of the metallic fuel rodlets (dimensions in inches) [10] (figure courtesy of Idaho National Laboratory).

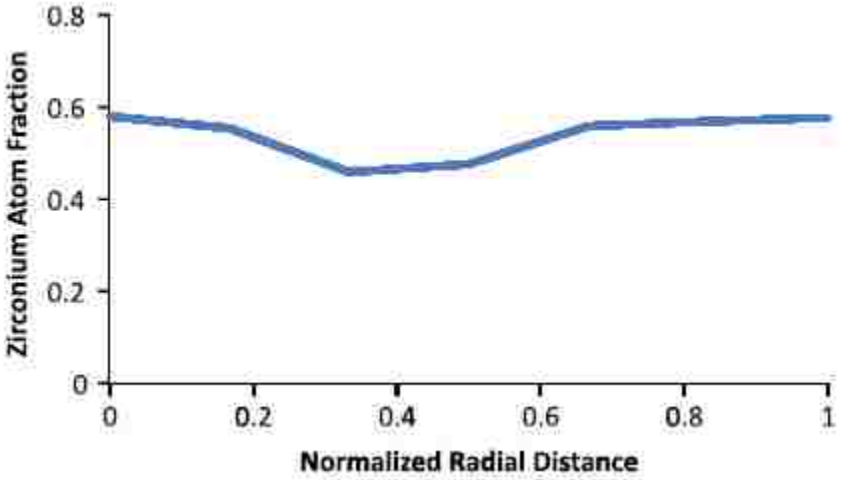

Figure 8. AFC-1F Zirconium Redistribution

Figure 8 represents the radial zirconium atom fraction results obtained experimentally. In this study (Figure 9), we have modeled the zirconium migration in another AFC rodlet, the AFC-1D rodlet 1. It has a similar composition to the 1F rodlet in Figure 8. Note that the result is again in good agreement. This 1D fuel contains approximately 40 wt% Zr.

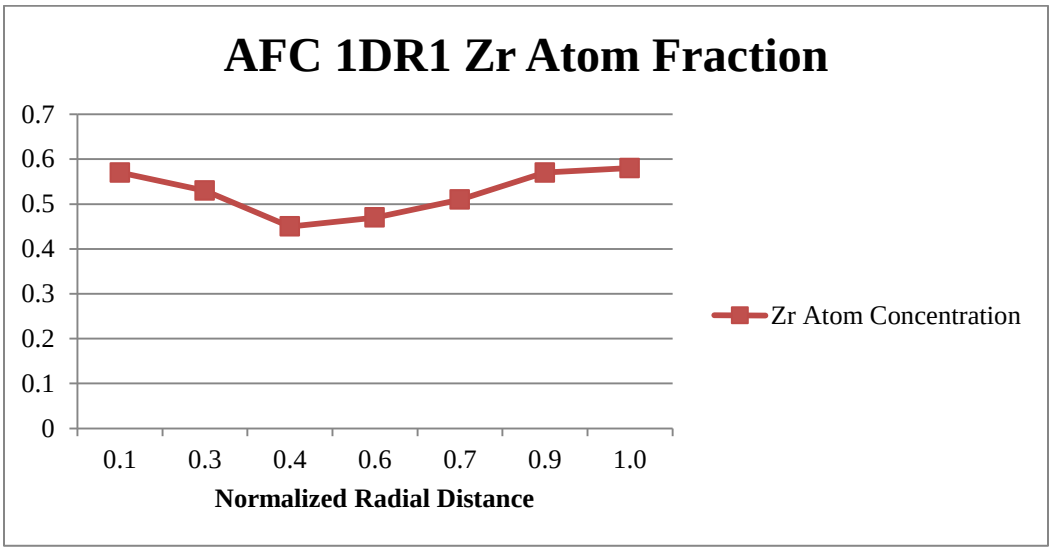

Figure 9. AFC 1DR1 Zr Atom Fraction

In Figure 10, radial heat generation rate (volumetric power) is plotted for the T473 EBR-II pin. It is useful to note that the curve is virtually the inverse of the zirconium atom fraction curve for the same pin.

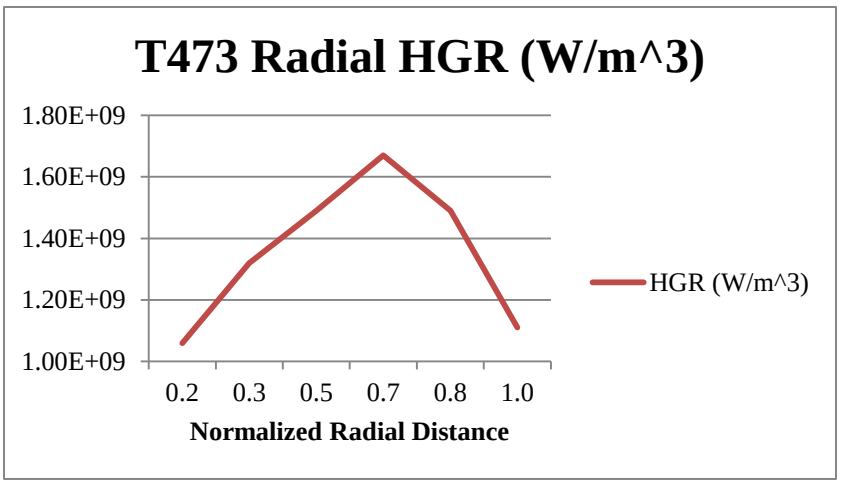

Figure 10. T473 Radial (Volumetric) HGR

CHAPTER 6. DISCUSSION AND CONCLUSIONS

The results presented in the previous chapter confirm several assumed characteristics of actinide and constituent diffusion/redistribution in metal fuels:

1. Pu does not migrate; hence, the U and Zr concentration profiles are proportionally opposite each other.
2. The equilibrium phases of the ternary U-Zr-Pu system are described by using a quasi-binary U-Zr phase diagram (with constant Plutonium content), which is produced from ternary phase diagrams, assuming uniformity of Plutonium in each phase of the multiphase zones.
3. The minimum allowed Zirconium concentration in the Zirconium depleted middle region is 5 atom % due to the solubility limit. When the concentration of a radial node drops below 5 atom %, further diffusion from this node to the adjacent nodes is not allowed. This limit corresponds to depletion of the matrix phase in the middle region.
4. The presence of plutonium in the alloy at levels greater than 8 wt% enhances uranium and zirconium migration by an order of magnitude.
5. Only radial migration of zirconium is considered. Axial temperature gradients are relatively small and axial zirconium redistribution has not been observed experimentally.
6. The radial power distribution in the fuel slug is demonstrated to be directly proportional to the actinide concentration distribution, and inversely proportional to the zirconium concentration distribution.

In the first phase of this work, a sensitivity study was performed on the thermo-mechanical models of FEAST-Metal, producing a reduced set of calibration parameters for possible adjustment in follow-on studies. A modification was then made to the constituent redistribution model to enable the code to properly handle metallic fuel with composition similar to that of AFC fuel.

Constitutive models in the FEAST-METAL fuel performance code have been extended to simulate high zirconium and low content minor actinide bearing, high fissile density metallic fuels. Approximate correlations have been adopted for constituent heats of transport, fuel thermal conductivity, modulus of elasticity, and thermal expansion coefficient. Experimental and theoretical observations support that the new fuel is stiffer than the low Zr bearing reference fuel. In other words, in high-Zr content fuel, the zirconium does not migrate nearly as much as in the low-Zr fuels. Also, once fuel becomes restricted by the cladding (due to swelling at higher porosity), pore sintering to accommodate solid fission product swelling occurs at a much higher level than low Zr fuel. This could potentially be resulting in excessive straining of the cladding and resulting fuel failures which have been observed [16]. The resulting FEAST-Metal fuel performance code could be used for design of transmutation reactor fuels for sodium fast reactor applications.

The addition of americium, neptunium, and curium to the traditional metallic fuel is considered in the Advanced Fuels Campaign. These actinides add further complications to the fuel behavior. For example, it is known from limited data that americium acts like zirconium and diffuses toward the center of the fuel with slower rates. Neptunium is observed to act like plutonium, which does not significantly diffuse. The weight fractions of uranium, plutonium, zirconium, americium, and neptunium in the AFC fuels vary.

Proposed/Future Work

It is highly desirable to develop a robust and reliable 3D predictive M&S tool set for metallic fast reactor fuel. To that end, it is recommended that development of INL's BISON-Metal code be taken to completion.

REFERENCES

1. A. Karahan, J. Buongiorno; “Modeling of Thermo-Mechanical and Irradiation Behavior of Metallic and Oxide Fuels for Sodium Fast Reactors.” MIT Center for Advanced Nuclear Energy Systems, August 2009.
2. P. Edelmann, B. Williams, A. Yacout, C. Unal; “Sensitivity Analysis of FEAST-Metal Fuel Performance Code: Initial Results.” Los Alamos National Laboratory, June 2012.
3. A. Karahan, J. Buongiorno; “Extending FEAST-METAL for Analysis of Low Content Minor Actinide Bearing and Zirconium Rich Metallic Fuels for Sodium Fast Reactors.” MIT Center for Advanced Energy Studies, October 2010.
4. A. Yacout, B. Williams, C. Unal, "Sensitivity Analysis Using LIFE-4 Fuel Performance Code," Los Alamos National Laboratory report, LA-UR-10-06575, September 2010.
5. A. Saltelli, K. Chan, and E. M. Scott, Sensitivity Analysis, John Wiley & Sons, 2000.
6. I. M. Sobol', "Sensitivity Analysis for Non-linear Mathematical Models," Mathematical Model. Comput. Exp., 1, 1993, pp. 407-414.
7. M. Lamboni, H. Monod, and D. Makowski, "Multivariate Sensitivity Analysis to Measure Global Contribution of Input Factors in Dynamic Models," Reliability Engineering and System Safety, 96, 2011, pp. 450-459.
8. Y. S. Kim et al., “Modeling of Constituent Redistribution in U-Pu-Zr metallic Fuel,” Journal of Nuclear Materials, Vol. 359, pp. 17-28, (2006).
9. T. Ogata et al., “Constituent Migration Model For U-Pu-Zr Metallic Fast Reactor Fuel,” Vol. 104, pp. 37-51, (1993).
10. B.A. Hilton, D.L. Porter, S.L. Hayes, AFC-1 Transmutation Fuels Post-Irradiation Hot Cell Examination 4 to 8 at.% Final Report, INL/EXT-05-00785, Rev. 1, 2006.
11. G. L. Hofman et al., “Temperature Gradient Driven Constituent Redistribution in U-Zr Alloys,” Journal of Nuclear Materials, Vol. 227, pp. 277-286, (1995).

12. W. Hwang et al., “Recent Improvements in Modeling Fission Gas Release and Rod Deformation on Metallic Fuel in LMR,” Vol. 27, pp. 1057-1069, (2000).
13. C. Newman, G. Hansen, and D. Gaston, “Three Dimensional Coupled Simulation of Thermodynamics, Heat, and Oxygen Diffusion in UO_2 Nuclear Fuel Rods,” *Journal of Nuclear Materials* **392**, 6–15 (2009).
14. B. Michel, J. Sercombea, G. Thouvenina, and R. Chateleta, “Local Approach to Fractures,” *Engineering Fracture Mechanics* **75**:11, 3581–3598 (July 2008).
15. J. Sercombe, B. Michel, G. Thouvenina, B. Petitprez, R. Chatelet, D. Leboulch, and C. Nonon, “Multi-Dimensional Modeling of PCMI during Base Irradiation and Ramp Testing with ALCYONE V1.1,” Proceedings of Top Fuel 2009, Paris, France, September 6–10, 2009, Paper 2096.
16. H. J. MacLean Chichester, D. L. Porter, B. A. Hilton, "Post-irradiation Examination of AFC-1D, 1G, 1H, and 2A Experiments," Idaho National Laboratory, September 2011.
17. A. Karahan, “Modeling of Thermo-mechanical and Irradiation Behavior of Metallic and Oxide Fuels for Sodium Fast Reactors,” Ph. D. Thesis, Nuclear Science and Engineering Department, Massachusetts Institute of Technology, Cambridge, MA, (2009).
18. D. C. Crawford et al., “Fuels for Sodium-Cooled Fast Reactors: US Perspective,” Journal of Nuclear Materials, Vol. 371, pp. 202-231, (2007).
19. N. E. Todreas et al., “Nuclear Systems-II, Elements of Thermal-hydraulic Design,” Taylor & Francis, (1990).
20. G. Strang, “Linear Algebra and its Applications,” Brooks/Cole Pub. Co., (1988).
21. C. B. Lee et al., “Fission Gas Release and Swelling Model of Metallic Fast Reactor Fuel,” Journal of Nuclear Materials, Vol. 288, pp.29-42, (2001).
22. T. Ogata et al., “Development and Validation of ALFUS: An irradiation Behavior Analysis Code for Metallic Fast Reactor Fuels,” Nuclear Technology, Vol. 128, pp. 113-123, (1999).
23. Y.S. Kim, G.L. Hofman, AAA Fuels Handbook, ANL-AAA-068, Argonne National Laboratory, 2003.

APPENDICES

A. GLOBAL SENSITIVITY ANALYSIS

We summarize an approach to variance-based global sensitivity analysis commonly used with complex computational models [5]. Let $\eta(\boldsymbol{z})$ denote code output calculated at input $\boldsymbol{z}$. Here $\boldsymbol{z}$ contains all inputs being varied, including operating and calibration parameters. We assume uncertainty in $\boldsymbol{z}$ is described by the probability density function (PDF) $g(\boldsymbol{z})$. Let I denote an index set of elements in $\boldsymbol{z}$, and $-I$ the complement index set of elements in $\boldsymbol{z}$ not in I. The conditional PDF $g(\boldsymbol{z}_I \mid \boldsymbol{z}_{-I})$ describes uncertainty in $\boldsymbol{z}_I$ given particular values for $\boldsymbol{z}_{-I}$.

It has been shown [6] that there is a unique decomposition

$$\eta(z_1,\ldots,z_d) = \eta_0 + \sum_{k=1}^{d} \eta_k(z_k) + \sum_{1\le k<l\le d} \eta_{kl}(z_k,z_l) + \ldots + \eta_{12\ldots d}(z_1,\ldots,z_d)$$

in which

1. $\eta_0 = \int \eta(z)\, g(z)\, dz = E_g[\eta(z)]$ is the expected value of the code output with respect to the assumed uncertainty in the inputs $\boldsymbol{z}$,
2. the remaining components have zero expected value, $E_g[\eta_I(z_I)] = \int \eta_I(z_I)\, g(z)\, dz = 0$, and
3. any two distinct components are orthogonal, $E_g[\eta_I(z_I)\eta_J(z_J)] = \int \eta_I(z_I)\eta_J(z_J)\, g(z)\, dz = 0$ for $I \neq J$.

Explicit expressions for each component are available. For example, the main effect for code input k is given by

$$\eta_k(z_k) = E_g[\eta(z) \mid z_k] - \eta_0 = \int \eta(z) g(z_{-k} \mid z_k)\, dz_{-k} - \eta_0.$$

The two-factor interaction effect for code inputs k and l is given by

$$\eta_{kl}(z_k,z_l) = E_g[\eta(z) \mid (z_k,z_l)] - \eta_k(z_k) - \eta_l(z_l) - \eta_0,$$

where $E_g[\eta(z) \mid (z_k,z_l)] = \int \eta(z) g(z_{(-k,-l)} \mid (z_k,z_l))\, dz_{(-k,-l)}$. In a similar fashion, higher order effects $\eta_I(z_I)$ with I having more than two elements are constructed by computing the joint effect

$$E_g[\eta(z) \mid z_I] = \int \eta(z) g(z_{-I} \mid z_I)\, dz_{-I}$$

and then subtracting all the lower order effects formed from elements of I.

With these definitions in hand, we turn our attention to the subject of primary interest, variance-based global sensitivity analysis. The total variance of code output $\eta(\boldsymbol{z})$ with respect to uncertainty in $\boldsymbol{z}$ is defined in the usual way,

$$V = \int \eta(z)^2 g(z)\, dz - \eta_0^2,$$

while the variance of individual components $\eta_I(z_I)$ in the Sobol' decomposition are computed as follows,

$$V_I = \int \eta_I^2(z_I) g(z_I) dz_I .$$

The sensitivity index corresponding to the effect $\eta_I(z_I)$ is defined to be the variance ratio $S_I = V_I / V$. If the inputs are taken to be independently distributed, then the total output variance decomposes into a sum of the component variances,

$$V = \sum_{k=1}^{d} V_k + \sum_{1 \le k < l \le d} V_{kl} + \ldots + V_{12\ldots d},$$

referred to as the analysis of variance (ANOVA) decomposition. The total effect of input *k* is defined as follows,

$$V_{T_k} = V - V_{-k},$$

that is, the total output variance minus the joint effect variance of all inputs except *k*. When the ANOVA decomposition holds, this simplifies to

$$V_{T_k} = V_k + \sum_{l \ne k} V_{kl} + \ldots + V_{12\ldots d},$$

which is the sum of input *k* main effect variance V_k and all interaction effect variances involving input *k*.

The calculated outputs from FEAST-Metal are functional, in that each input setting results in an output curve in time. Global sensitivity analysis for functional outputs is conducted in a straightforward fashion by converting the functional output into an equivalent (with respect to sensitivity analysis) scalar output using principal component analysis. The steps are as follows:

1. If necessary, interpolate the output from each input setting onto a common time grid.
2. Compute the output correlation matrix **P**.
3. Orthogonalize **P** to obtain **P** = **VΛV**', where **V** is the matirix of (column) eigenvectors and **Λ** is the diagonal matrix of associated eigenvalues.
4. Obtain the matrix of principal component *scores*, **H**(**X**), as **H**(**X**) = **V**'**η**(**X**), where **X** is the matrix of input settings in the experiment design and **η**(**X**) denotes the matrix of corresponding mean-centered and standard deviation-scaled outputs.
5. Construct the scalar output **h**(**X**) by summing across the columns of **H**(**X**), and conduct global sensitivity analysis on **h**(**X**).

It can be shown [7] that the variance components computed from scalar **h**(**X**) are equivalent to the generalized variance components computed from the full functional data **η**(**X**).

B. DESCRIPTION OF TEST FUEL

EBR-II Fuel

X425 Test Array (T179, T473):

Parameter	Value
Fuel Composition	U-19-Pu-10Zr
Clad Material	HT-9
Fuel slug radius (mm)	2.16
Clad inner radius (mm)	2.54
Clad outer radius (mm)	2.92
Fuel Smear Density (%)	72.4
Fuel Active Length (cm)	34.3
Plenum to Fuel Ratio	1.0
Peak Linear Heat Rate (kW/m)	40
Peak Clad Temperature (deg C)	590

AFC Fuel

1D-Rodlet 1

Rodlet Length (in.)	5.997
Rodlet OD (in.)	0.230
Rodlet Mass (g)	16.403
Fuel Column Length (in.)	1.490
Fuel OD (in.)	0.152
Fuel Mass (g)	4.443
Fuel Density (g/cm3)	9.917
Fuel Nominal Composition	48Pu-12Am-40Zr
Pu (wt%)	48.36
239Pu (%)	82.57
240Pu (%)	16.51
241Pu (%)	0.57
Np (wt%)	0.25
Am (wt%)	11.90
Zr (wt%)	40.00
Na Mass (g)	0.49